Hierarchical multi-scale models for mechanical response prediction of highly filled elastic-plastic and viscoplastic particulate composites

J. Y. S. Li-Mayer[a], D. Lewis[b], S. Connors[b], A. Glauser[b], D.M. Williamson[c], H. Arora[d] and <u>M. N. Charalambides</u>[a]

[a] Department of Mechanical Engineering, Imperial College London, SW7 2AZ, UK

[b] AWE, Aldermaston, Berkshire, RG7 4PR, UK

[c] The Cavendish Laboratory, Physics Department, University of Cambridge, Cambridge, CB3 0HE, UK

[d] Zienkiewicz Centre for Computational Engineering, College of Engineering, Swansea University, SA1 8EN, UK

Corresponding author: m.charalambides@imperial.ac.uk

1   **Abstract**

2   Though a vast amount of literature can be found on modelling particulate reinforced composites and

3   suspensions, the treatment of such materials at very high volume fractions V_f (>90 %), typical of high

4   performance energetic materials, remains a challenge. The latter is due to the very wide particle size

5   distribution needed to reach such a high value of V_f. In order to meet this challenge, multiscale

6   models that can treat the presence of particles at various scales are needed. This study presents a

7   novel hierarchical multiscale method for predicting the effective properties of elasto-viscoplastic

8   polymeric composites at high V_f. Firstly, simulated microstructures with randomly packed spherical

9   inclusions in a polymeric matrix were generated. Homogenised properties predicted using the finite

10   element (FE) method were then iteratively passed in a hierarchical multi-scale manner as modified

11   matrix properties until the desired filler V_f was achieved. The validated hierarchical model was then

12   applied to a real composite with microstructures reconstructed from image scan data, incorporating

13   cohesive elements to predict debonding of the filler particles and subsequent catastrophic failure.

14   The predicted behaviour was compared to data from uniaxial tensile tests. Our method is applicable

15   to the prediction of mechanical behaviour of any highly filled composite with a non-linear matrix,

16   arbitrary particle filler shape and a large particle size distribution, surpassing limitations of

17   traditional analytical models and other published computational models.

18   **1.0 Introduction**

19   Polymer bonded explosives (PBX) are highly filled particulate composites, consisting of a rigid filler

20   phase and a relatively compliant polymeric phase. A range of different explosive crystals and

21   energetic matrix binders are used in a variety of combinations and research in PBX has aimed to

22   understand and predict the mechanical and chemical performance of each formulation (An et al.,

23   2013; Anoop, 2013; Barua et al., 2012b; Drodge et al., 2010; Guo et al., 2014; Lin et al., 2015; Xiao et

24   al., 2012; Yeager, 2011, Barua and Zhou, 2011). Such studies are needed in order to increase the

25   safety of these materials in civil and military applications. The challenges in predicting the

26   mechanical behaviour of PBXs up to failure are due to the filler volume fraction (V_f) which can be in

27   excess of 90 % (Banerjee and Adams, 2004), the highly non-linear, time-dependent behaviour of the

28   matrix phase (Drozdov, 1999; Williamson et al., 2008) and the complex behaviour of the interface

29   between the filler and matrix phases (Bailey et al., 1992; Tan et al., 2005; Xu et al., 2008). The

30   damage mechanisms within and between the individual constituents and their contributions to

31   macroscopic failure under a multitude of loading conditions including tension and compression in

32   dynamic and quasi-static conditions continues to be a topic of current research interest (Ellis et al.,

33   2005; Herrmann et al., 2015; Li et al., 2005; Liu et al., 2009; Wang et al., 2011; Yeager et al., 2014;

34   Zhou et al., 2011).

35   Regardless of the computational method used to simulate the mechanical response of PBX,

36   generating a geometrical representation of the microstructure for such high volume fractions (filler

37   V_f >90 %) is yet an unsolved problem.

38   In the actual composites, high V_f values (>90 %) are only possible due to the wide range of particle

39   sizes. Progressively smaller particles are used to fill the remaining gaps between the larger particles

40   and theoretically a V_f tending to 100 % can be achieved. The maximum random packing V_f using

41   mono-disperse spheres is 63.7 % (Kansal et al, 2002) and using five classes of particle sizes and

42   particle size distribution of actual composites, V_f of 65% and 66% have been achieved respectively

43   (Annapragada et al., 2007; Baer, 2002). Hermann et al. using a packing technique of adding

44   progressively smaller spheres, achieved a maximum packing fraction of 95 % (Herrmann et al., 2003).

45   However, due to meshing restrictions, only V_f up to 70 % has been modelled using the FE method

46   (Jalocha et al, 2013). There comes a point where the smallest particles would require elements so

47   small that even with mesh decimation, the developed model is too inefficient to be used for design

48   and exploration purposes. Brouwers suggested that the ratio of the largest and smallest particle

49   radii, α, should be <10 (Brouwers, 2006) and found the maximum V_f for poly-dispersed spheres

50   where α =10 to be 67.2 %.

51   An alternative method for generating high filler V_f microstructures is the use of the Voronoi

52   tessellation method to pack conforming polygons (Seidel et al., 2005; Wang et al., 2016; Wu and

53   Huang, 2009). Using this method, previous researchers have achieved a maximum V_f of 82 % (Barua

54   et al., 2012a) and 90% (Wang et al., 2016). To achieve a V_f above 90 %, previous researchers have

55   also incorporated the binder material behaviour into the cohesive constitute law, essentially

56   modelling both the binder matrix material and the filler-matrix interface as one entity (Guo et al.,

57   2014; Wu and Huang, 2009).

58   However, the Voronoi tessellation method places restrictions on the filler size distribution, which is

59   notorious for its significant effect on the predicted composites behaviour (Marvi-Mashhadi et al,

60   2018a,b). The use of fine and coarse particles can affect the mechanical properties and specifically

61   the mechanical strength and elongation properties of the composites (Arora et al, 2015; Talawar et

62   al., 2006; Willey et al., 2009). Representative Volume Elements (RVEs) generated via Voronoi

63   tessellation uses seed points generated from the centres or random close-packed sphere

64   distributions; the method is not therefore always able to reproduce a prescribed, broad range, size

65   distribution though the latter may be accomplished by means of a Laguerre tessellation (Marvi-

66   Mashhadi et al, 2018a,b). The latter gives the extra freedom to weight each seed point such that it

67   will control the volume of the corresponding cell. Even so, modelling the interface and the matrix

68   together in one constitutive model, does not allow sufficient mathematical description of the

69 different mechanical response and damage mechanisms occurring in the interface and matrix

70 regions.

71 Experimental studies on PBXs found that debonding first occurs around the larger particles and that

72 the 'lost' smaller particles only contribute to the stiffening of the matrix material (Rae et al., 2002).

73 This has been further confirmed by a multi-scale damage computational model to investigate the

74 effect of particle size and interaction effects in highly filled particulate composites (Trombini et al.,

75 2015). If only the mechanical properties of the composite up to the initial stages of failure are of

76 interest, then based on this finding, it is possible to treat the matrix material with small embedded

77 particles as a microscopic scale model. The determined homogenised behaviour of the microscopic

78 scale model is then validly representative of the matrix behaviour in the macroscopic scale model.

79 This decoupled multi-scale approach, otherwise known as a hierarchical or sequential multi-scale

80 model would be suitable in this instance (Aboudi et al., 2013). Based on this assumption, the

81 polymeric matrix used in a PBX together with the smaller 'lost' particles is often termed the fine

82 loaded binder (FLB), and offers an alternative way of modelling such high filled composites.

83 Banerjee and Adams, (Banerjee and Adams, 2004) have also employed a similar idea to the FLB

84 method, to predict the composite elastic modulus for V_f higher than 90 % using a 2D randomly

85 packed model with spherical inclusions. Yet, this concept has still not been validated against finite

86 element predictions and experimental results for plastic or viscoplastic binders such as the ones

87 studied here. Another example based on the FLB assumption is by Arora et al. (Arora et al., 2015)

88 who predicted the tensile behaviour of a viscoelastic PBX with a 95.1 % filler V_f reconstructed 2D

89 microstructural finite element models from SEM images. The smaller particles were lost during

90 image processing and the filler V_f of the segmented image was only 57 %. Arora et al. considered the

91 smaller 'lost' particles (<50 μm) to be embedded in the matrix binder and incorporated the effect of

92 the lost filler particles into the matrix (FLB). The resulting homogenised properties were then

93 determined using a viscoelastic extension of the Mori-Tanaka analytical model (Mori and Tanaka,

94 1973). This assumption has not yet been validated though.

95 The aim of this research was to compare for the first time the decoupled multi-scale homogenisation

96 method, also known as hierarchical method, to the FLB or 'dirty' binder method (Arora et al., 2015;

97 Banerjee and Adams, 2004), for predicting the mechanical behaviour of highly filled binary

98 composites (>90 %). The method is applied to a PBX with an elastic-viscoplastic matrix. The outline

99 of the paper is as follows: firstly, the details of the materials and the mechanical characterisation of

100 the matrix and the binder are presented in section 2, followed by the microstructure analysis of the

101 composite (section 3). Section 4 presents the image based numerical model setup for predicting the

102 mechanical response of the PBX. In this model, the 'matrix' is in fact the fine loaded bunder (FLB)

103   which is later defined through the FLB homogenisation described in section 5 through a novel multi-

104   scale FE model. Some analytical micromechanical models used to compare to the numerical

105   predictions are given in Section 6. The results from the multi-scale FE models of section 5 are

106   examined and validated against predictions from single-scale FE models for V_f up to 72 % in sections

107   7.1 and 7.2. Section 7.3 investigates the predictions from the image-based model of the actual PBX,

108   making use of the multi-scale FLB model. Finally, section 8 summarises the study's findings. The

109   work presented here enables modelling of very highly filled particulate composites which have so far

110   proven to be extremely challenging. The modelling method developed provides an efficient and

111   powerful design tool for use by industry and composite manufacturers.

112

113   **2.0 Mechanical characterisation of the binder and the composite materials**

114   In this section, details of the material used as well as the tests performed to characterise the binder

115   and the composite are described.

116   **2.1 Materials and experimental methods**

117   The PBX consists of a compliant fluorocarbon matrix, FK800, and rigid triamino-trinitrobenzene

118   (TATB) filler particles. FK800 is a random copolymer of 75 % w.t. Chlorotrifluoroethylene (CTFE) and

119   25 % w.t. Vinylidene Fluoride (VDF). The molar mass of CTFE and VDF, are 64.2 g/mol and 116.47

120   g/mol respectively, resulting in a semi-crystalline copolymer with a 38 % mole fraction of VDF and a

121   density of 2 g/cm^3 (Connors, 2014). The glass transition temperature of the binder polymer as

122   measured from the peak in loss tangent from Dynamic Mechanical Analysis data (data not shown)

123   was 34 °C. Its crystallinity was not measured but is reported to be approximately 10% in the

124   literature and highly dependent on the thermal history of the sample (Hoffman et al, 1989). The PBX

125   is formed by mixing the dry blend of crystal wetted with solvent and the binder to form a moulding

126   powder granule (Banerjee and Adams, 2004). The powder is then isostatically compressed at high

127   temperature until the porosity is reduced to 1-2 %. The filler volume fraction was 95% based on the

128   mass fractions and density values of the constituents. The material is considered macroscopically

129   isotropic as it composed of randomly oriented crystals with no preferred direction (Xiao et al,

130   2007).

131   The TATB filler is a widely studied explosive with both its adhesive and mechanical properties

132   reported in the literature (e.g. Qin et al, 2019, Xiao et al, 2005, Gee et al, 2007). TATB has a

133   crystalline structure and under high shear forces fracture may initiate at planes of preferred slip. This

134   was not considered in the current study as fracture along the crystal/matrix interface is the primary

135   failure mechanism of interest with crystal fracture being a secondary mechanism (Guo et al, 2014).

136 In addition, it is impossible to obtain information on the crystal orientation and the associated

137 anisotropy using 2D images alone as we have here (Figure 2). For these reasons as well as to keep

138 the model as simple as possible, isotropic elastic properties were assumed here for the filler and

139 were taken from literature with modulus, E^*, Poisson's ratio, ν^* and density, ρ^* defined to be 31.5

140 GPa, 0.2 and 1.94 g/cm^3 respectively (Arora et al., 2015).

141 In order to characterise the matrix, monotonic uniaxial tensile tests were performed at 20°C and

142 arbitrary true strain rates of 0.14 /s and 0.0014 /s with three repeats using dumbbell shaped

143 specimens of dimensions in accordance with British Standard BS EN ISO 527-2:2012 (type A) (BSI,

144 2012). The true strain rate was kept constant via exponentially decreasing the crosshead rate of the

145 tensile testing machine (Zwick/Roell Z 1.0). Five reference lines were drawn across the gauge length

146 to examine the strain along the gauge length as shown in Figure 1(a). The sample deformation

147 corresponding to three different levels of strain (0.05, 0.5 and 0.7) are shown. Several such image

148 data were collected and processed using MATLAB to measure strain along the sample. The images

149 were specifically analysed using the MATLAB line tracker tool, which registers points of negative

150 greyscale contrast (ie lines) as minimums in a greyscale intensity plot. The changing distance

151 between successive minimums was used to determine the strain along the sample.

152 For the composite, uniaxial tensile loading at a true strain rate of 0.00005 /s was applied to five

153 cylindrical dumbbell specimens machined from a pressed billet. The samples had an average axial

154 gauge length and diameter of 12 cm and 3.8 cm respectively. They were tested until failure at 20 °C.

155 Two clip strain gauges were used at either side of the sample in order to check against bending

156 effects as well as control the crosshead displacement for true strain rate loading. Only uniaxial

157 tensile tests were performed in this study; testing the composite under uniaxial compression would

158 have provided further data for validating the models presented in the following sections. In addition,

159 such additional tests would have revealed any pressure dependency of the damage and fracture

160 behaviour of the composite through the effective variation in the applied triaxiality factor

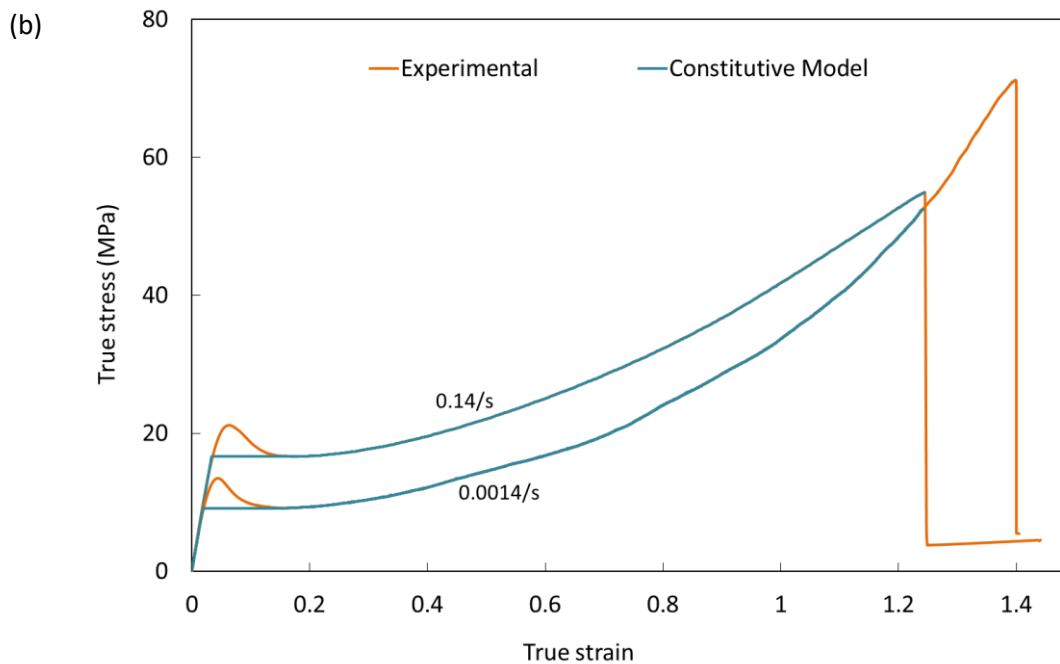161 (Skamniotis et al., 2019)

162

163 **2.2 Mechanical characterisation results**

164 Image data was collected and processed using MATLAB and the strains measured for each segment

165 were found to be uniform. The true stress- true strain results are shown in Figure 1(b).

166

(a)

strain=0.05

strain=0.5

strain=0.7

167

(b)

168
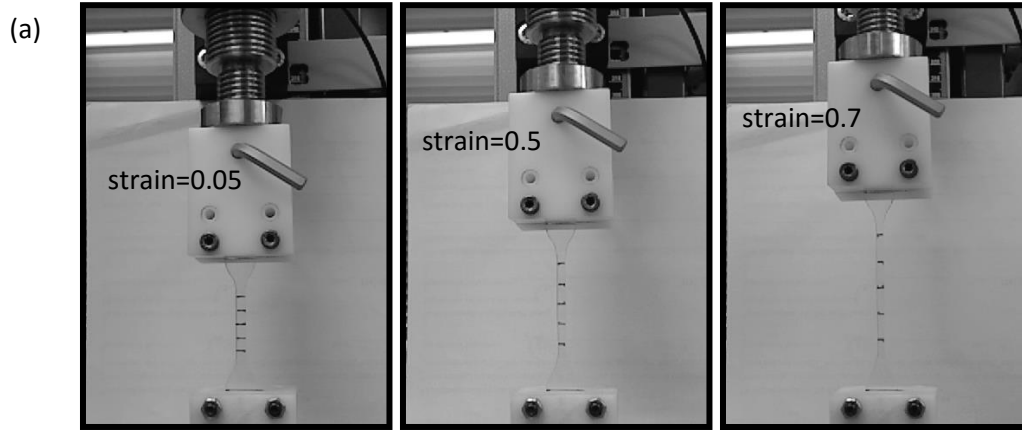
Figure 1: (a) Images of sample deformation during the tensile test corresponding to three different
levels of strain: 0.05, 0.5 and 0.7; marked lines were used to estimate the strain along the sample
to check for uniform loading conditions, (b) Uniaxial tension test data of FK800 at two strain rates
(0.14 /s and 0.0014 /s); the constitutive model used in the FE models is also shown for
comparison.

The yield stress, σ_Y , was observed to be strain-rate dependent. However, no such significant

observation was noted for the initial slope. Therefore, the classic isotropic von-Mises plasticity with

strain hardening and rate dependent yielding was used to model the binder's elasto-viscoplastic

behaviour. The Young's modulus was set to a value of $E = 500$ MPa, the Poisson's ratio was taken

as $v = 0.38$ (Wood et al, 2017) and the rate dependent yield stresses were set to $\sigma_Y(\dot{\varepsilon} = 0.0014) = 9.15$ MPa and $\sigma_Y(\dot{\varepsilon} = 0.14) = 16.6$ MPa. Post yield, the stresses are defined as a

function of plastic strain (total strain minus the elastic strain) in a tabular form for each of the two

strain rates (Abaqus 6.14, SIMULIA). A strain softening region was observed in the tensile stress-

183   strain response measured prior to the strain hardening region. This was thought to be due to the

184   storage of the material for a long period of time prior to testing (approximately six months), which

185   allowed re-arrangement of polymer chains over time and resulted in an increased amount of

186   crystallisation (Cady and Caley, 1977, Hoffman et al, 1989). In the high-volume fraction, hot pressed

187   composite, the matrix binder thickness is so small that the formation of crystals is restricted;

188   crystallinity has been reported to drop to less than 1% (Connors, 2014). On the other hand, it is also

189   possible that the peak stress could also be due to ageing of the amorphous phase that would be

190   present in the material too. In an effort to keep the model as simple as possible, the strain softening

191   region was not included in the constitutive model for the binder, as shown in Figure 1(b).

192   For the composite, the measured elastic modulus ranged from 6.5-11.6 GPa with an average of 8.6

193   GPa and the stress and strain at failure ranged from 8.0-9.3 GPa and 0.0017-0.0022 with an average

194   of 8.2 GPa and 0.0017 respectively. The tensile true stress-strain behaviour of the composite up to

195   failure is shown later in Figure 13, taken from the average of all five specimens tested. The

196   fluctuations specifically for the modulus could be due to the relatively small elastic region

197   corresponding to extremely low strains (only 0.00025 in Figure 13).

198

199   **3.0 Microstructure of the composite material**

200   2D Image data of the TATB/FK800 composite were obtained using a Focussed Ion Beam microscope

201   (see Figure 2). The cut surfaces were uncoated, i.e. no metallisation was used. The surface was

202   bombarded with a beam of gallium ions which causes secondary electrons to be ejected. A co-axial

203   electron detector collected these ejections to form an image of the surface. This technique was

204   chosen as it improves contrast between the crystal and the binder. The beam settings were 30 kV

205   and 10 pA. The obtained image shows the outlines of the crystals as well as some defects within

206   them. The original image with a field of view (FOV) of 426 x 302 μm was segmented using image

207   processing software, Avizo (Visualization Sciences Group, Bordeaux, France/ Zeuss Institute Berlin,

208   Germany). The segmented image was binarised and divided into four smaller images with

209   dimensions of 144 x 105 (Figure 2). Volume fraction, particle statistics and particle size distribution

210   of the full image and the four sub-images (labelled as Volume Elements, VE1-VE4) were analysed

211   using MATLAB (Mathworks, Massachusetts, USA).

212

213
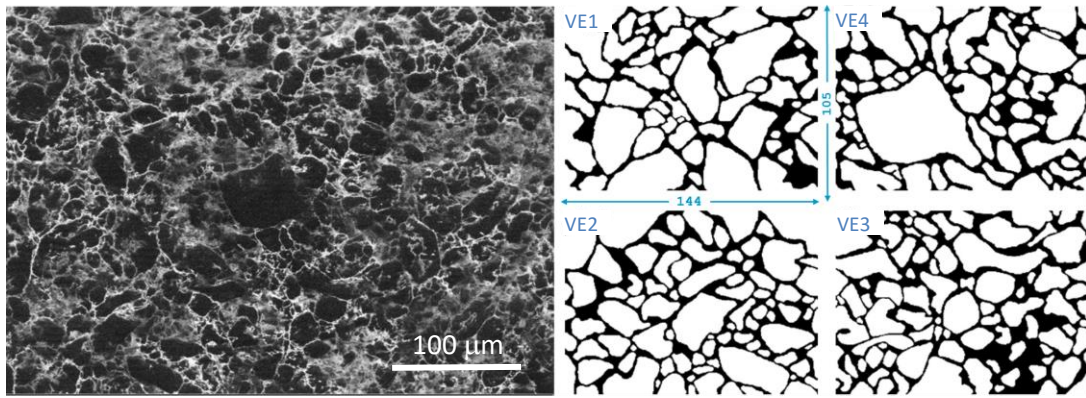
Figure 2 Focussed ion beam microscopy image data and the four sub-divided images of the TATB/ FK800 composite (dimensions in μm).

The particle size distribution, mean, maximum and minimum particle radius for all the four sub-images were found to be of the same order of magnitude as the full image (Table 1) and a skewed normal distribution was observed for the particle sizes, see Figure 3. The five distributions in Figure 3 are very similar, especially considering these are experimentally derived from images which were hard to segment due to the inherent lack of image clarity for this specific PBX. The agreement between the distributions corresponding to the four sub-VE's as well as to the bigger full-size image, together with the similar volume fractions shown in Table 1 (ranging from 66%-73%), justify considering each of these images as characteristic of the microstructure of the composite. Arora et al, 2015, studied a similar PBX; it was shown that model size did not play a significant role on the computed results based on data derived from a full image (157 μm x 222 μm) and four smaller sub-images of varying sizes all the way down to 1/16 of the original area.

In comparison to measurements obtained from sieve tests of the TATB crystals (BSIb, 2012), the minimum particle size measured in the segmented images was found to be significantly larger than that measured experimentally (see Table 1). This is partially due to the limitation on the imaging resolution. Further loss of the smaller particles arises during the segmentation and image processing stages, where small clusters of a few pixels are removed. The ratio of the largest to the smallest particle from the sieve test was observed to be in the order of 600.

The maximum particle size measured from the segmented images was found to be lower than the maximum particle size measured using the sieve analysis. This difference could be attributed to two causes. Firstly, only one arbitrary plane of the entire microstructure has been imaged in which the longest axis of the largest particle may not have been present. Secondly, particles might have fractured into smaller particles during manufacturing of the composite. In literature, a different particle size distribution has been observed post processing where the cumulative V_f of the finer

240 sized particles was higher (Skidmore et al. 1998) compared to the un-processed dry blend (Banerjee

241 and Adams, 2004). The same observation was made in this study where the mode of the segmented

242 images particle size distributions was lower than the mode of 11.8 µm measured from the sieve test.
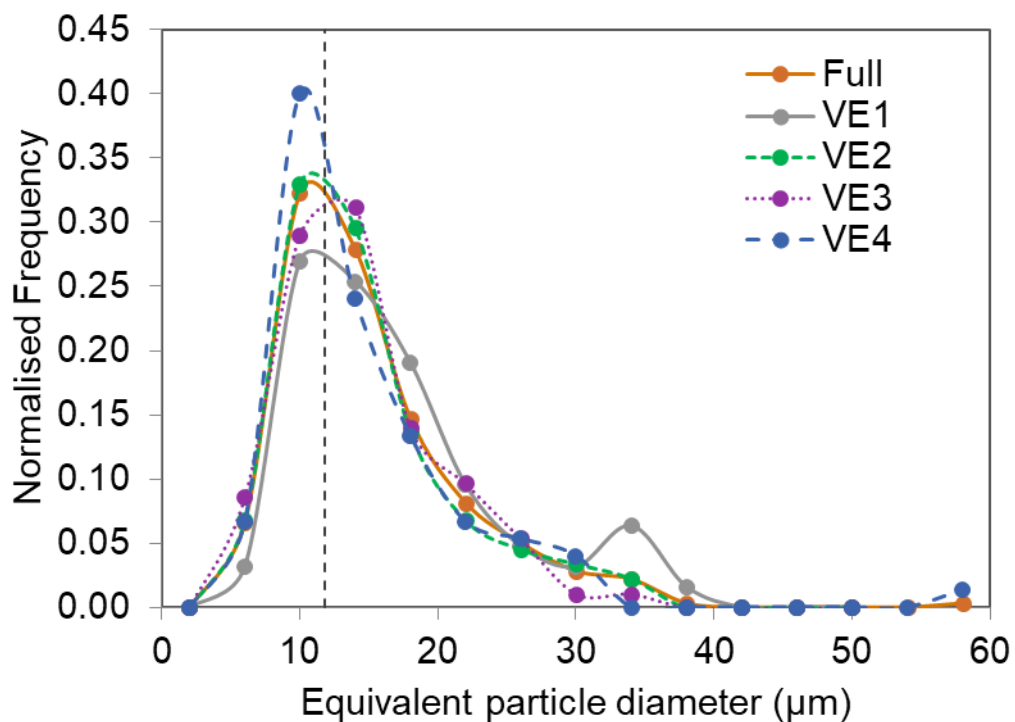
243

244 **Table 1 Particle statistics from sieve test and from image analysis of the segmented volume**
245 **elements.**

VE	Equivalent particle diameter (µm)				V_f	No. of particles
	Max.	Min.	Mean	Mode		
VE1	35.0	3.4	13.0	8.0	0.73	63
VE2	29.3	3.0	10.9	7.9	0.72	88
VE3	28.2	1.9	10.3	12.8	0.66	96
VE4	55.2	2.3	10.9	6.7	0.71	80
Full	55.2	1.9	11.1	12.8	0.71	320
Sieve test	83.4	0.145	-	11.8	-	-

246

247

248

249 **Figure 3 Particle size distribution analysis of the full and the four sub-volume elements. The grey**
250 **vertical dotted line depicts the mode from the sieve test (see Table 1).**

251

252 Finally, the four sub-images shown in Figure 2 were further analysed to quantify the thickness of the

253 matrix between particles using Matlab. The changes in greyscale intensity along random lines drawn

254 across the images were used to identify the boundaries of the filler and the matrix. It was found that

255   the thickness varied in the range of 0.67 - 15.7 μm with an average of 3.1 μm, agreeing with quoted

256   values for similar PBX materials (Arora et al, 2015).

257

4.0 Image-based numerical model for predicting the PBX composite behaviour

259   This section describes the development of the 2D plane strain image-based models for predicting the

260   mechanical response of the PBX. The latter is assumed to be a binary composite, with discrete TATB

261   particles embedded in the FK800 continuous matrix. The model allows for debonding to take place

262   at the matrix/particle interface using the cohesive zone approach.

263   Four FE models with the segmented microstructures were reconstructed from the binarised images

264   of the sub-VEs (VE1-VE4) shown in Figure 1, using a connectivity based algorithm to identify the

265   boundary of each particle approximated as a polygon (Tarleton et al., 2012). The particle/matrix

266   interfacial region is then produced by offsetting the boundary a small distance inwards and is

267   modelled by a single layer of cohesive elements. More details about the segmentation and meshing

268   process can be found in Tarleton et al., 2012. The same method has also been used to successfully

269   predict the mechanical response and failure strength of other particulate composites though those

270   were filled to much lower volume fractions (up to 45%) than the PBX materials studied here (Zhang

271   et al., 2018, Tarleton et al., 2013 and Mohammed et al, 2013.)

272   The resulting V_f of the four FE models were 72 %, 70 %, 65 % and 70 %. The FE models of the four

273   VEs were meshed with a total of 51-87k elements, the minimum required for mesh convergence,

274   and were analysed using the dynamic explicit solver in Abaqus 6.14 (SIMULIA, Rhode Island, USA).

275   The explicit solver was employed to avoid potential convergence difficulties arising due to softening

276   in the material response during the progressive damage of the cohesive zone elements (SIMULIA,

277   Rhode Island, USA). Four node cohesive elements, COH2D4, were used for the cohesive layer and

278   four node bilinear plane strain elements with reduced integration formulation and hourglass control,

279   CPE4R, were used for the matrix and the filler regions. A tensile strain of 0.0025 was applied at a

280   strain rate of 0.00005 /s to match the experimental strain rate (section 2.1) via prescribing a

281   displacement at the top surface; symmetric conditions were applied on the bottom surface whereas

282   the two side edges were constrained to remain straight during deformation. Periodic boundary

283   conditions were considered too but it was found that the results were similar to the 'straight'

284   boundary condition (Arora et al, 2015).

285   The TATB fillers were assumed to be linear elastic with the properties given in section 2.1.

286   A bi-linear uncoupled traction-separation cohesive law (see Figure 4) was used to describe the

287   matrix-particle interface behaviour. Damage initiation was defined based on a maximum stress

288   criterion defined by,

$$max\left\{\frac{\langle\sigma_n\rangle}{\sigma_n^o},\frac{\sigma_s}{\sigma_s^o}\right\} = 1 \qquad [1]$$

289   where σ_n^o and σ_s^o are the peak normal and shear contact stresses respectively when separation is

290   purely in their respective direction. These values were defined to be $\sigma_n^o = \sigma_s^o = 13$ MPa previously

291   used for materials of the same chemical composition (Arora et al., 2015). Stiffness of the cohesive

292   elements were also assumed to be equal in the normal and shear directions where, $K_n = K_s =$

293   315 GPa/μm as per Arora et al., 2015. The mode I, G_{Ia}, and mode II, G_{IIa}, fracture energies were

294   assumed to be equal for this study, $G_{Ia} = G_{IIa} = 0.271$ J/m^2, as determined by molecular dynamics

295   between TATB and FK800 (Gee et al., 2007; Ma et al., 2006), though these parameters could also

296   depend on the strain rate and temperature (Williamson et al., 2017). The mixed mode behaviour

297   was defined using the simple linear failure locus,

$$\frac{G_I}{G_{Ia}} + \frac{G_{II}}{G_{IIa}} = 1 \qquad [2]$$

298   where G_I and G_{II} are the energies released in mode I and mode II.
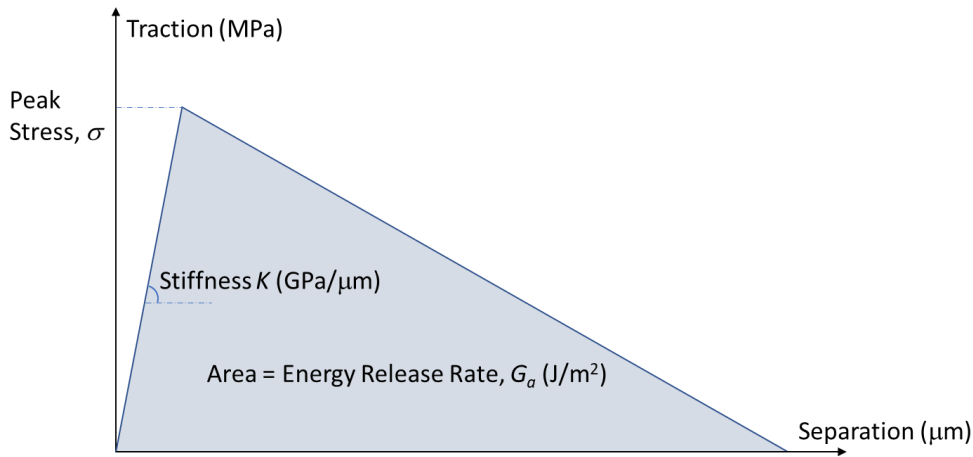
299

300   **Figure 4: Schematic of traction-separation cohesive zone law.**

301

302   As the microstructure images used to define the VEs of the FE models have values of V_f = 65-72 %

303   and the composite has a total V_f of 95 %, a V_f of 23-30 % of filler particles was 'lost' and therefore

304   not explicitly modelled. This 'lost' particle fraction is accounted for by using the multiscale model

305   described in section 5.0. Once this multiscale model is validated in sections 7.1 and 7.2, it will be

306   used to the define the matrix properties of the PBX composite model in section 7.3.
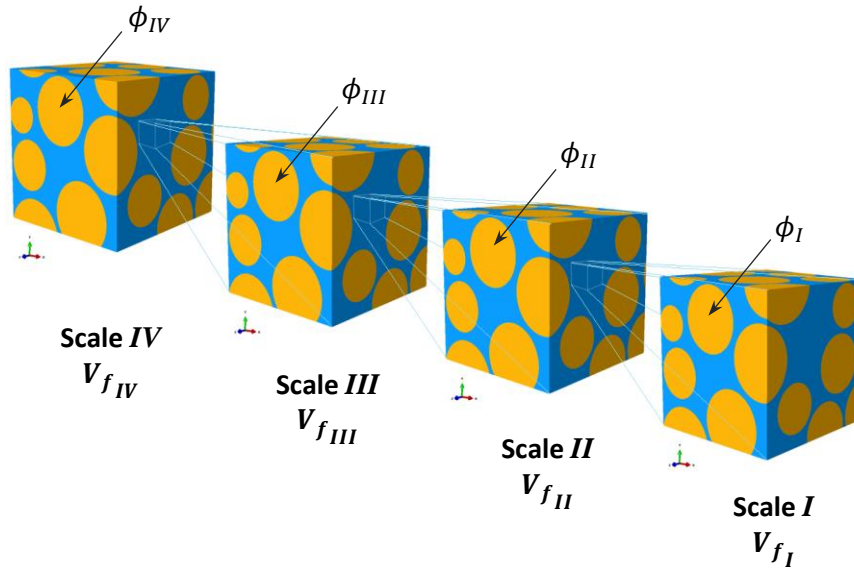
5.0 3D Hierarchical decoupled multi-scale FE models

The multi-scale decoupled method consists of a series of micromechanical FE models linked in a bottom-up manner. Figure 5 illustrates an example where four simulations at four different scales are used to model the high V_f of the real composite. In Scale I, spherical particles are embedded in a cubic RVE. The V_f at scale I, V_{f_I}, is $\emptyset_I$ % and all the fillers are modelled explicitly by the particles shown. At the next larger scale, Scale II, the RVE used also has embedded spherical particles and these make a V_f of $\emptyset_{II}$ %. At Scale II, the matrix properties are assigned the properties of those obtained from the Scale I model (i.e. E_I, ν_I and σ_{Y_I}). The total volume fraction of the Scale II model, $V_{f_{II}}$, is therefore given by,

$$V_{f_{II}} = \phi_{II} + V_{f_I}(1 - \phi_{II}) = \phi_{II} + \phi_I(1 - \phi_{II}) \quad \text{as } V_{f_I} = \phi_I \tag{4}$$

This hierarchical approach can be repeated n times until the total required volume fraction is incorporated. The total volume fraction model at any given scale, V_{fn}, is determined using the iterative formula,

$$V_{f_n} = \phi_n + V_{f_{n-1}}(1 - \phi_n) \quad \text{where } n = I, II, III..etc. \tag{5}$$

An elastic-plastic model was used for the matrix with $E = 500$ MPa, Poisson's ratio, $\nu = 0.38$ and yield stress, $\sigma_Y = 10$ MPa for the scale I model. These properties were selected to be very similar to the FK800 binder properties (see section 2.1). Even though the binder is elasto-viscoplastic, here no rate dependence was assumed to enable the accuracy of the hierarchical model to be studied in an efficient manner; rate dependence would have considerably increased the number of simulations needed due to the fact the homogenisation would need to be performed at each scale for various rates. Note however, that for the real composite simulation, the latter step was indeed followed for three rates at each scale, as will be discussed later in section 7.3. For Scales II and higher, the homogenised response of the composite from the previous scale was used to define the matrix material properties. For all scales, the fillers were assumed to be linear elastic with the properties

E^* = 31.5 GPa and ν^* = 0.2 (same properties as the TATB particles, see section 2.1).

Figure 5 Illustration of the hierarchical decoupled multi-scale FE method for modelling high volume fraction composites

This process was followed employing five distinct 3D periodic simulated cubic geometries summarised in Table 2 (models Rn a, Rn b, Rn c, Rn d and Rn e, where Rn in front of each model name denotes 'random'), with randomly dispersed spherical particles generated using a Monte Carlo simulation (Roskilly et al, 2010) at the arbitrary filler V_f of 11 %, 19 % and 29 % (MacroPac, Oxford Materials, UK). For the higher V_f of 36 % and 56 %, an overlap minimization packing algorithm was used for maximising packing efficiency (MacroPac, Oxford Materials, UK). No restrictions were specified for the inter-particle spacing (Gusev, 2016). The total volume of all five models is constant at L^3. The values of the volume fraction V_f, the ratio of the largest to smallest particle radii, α, the mean particle radius and its standard deviation, as well as the total number of spheres are given for each of the five models in Table 2.

Table 2 Packing parameters for the randomly packed volume elements in a cubic space of size L^3 ; α is the ratio of the largest to smallest particle radii.

V_f(%)	Model Name	α	Mean particle radius	Std. Dev.	No. of spheres
11	Rn a	1	0.08L	-	50
19	Rn b	1.7	0.05L	0.006L	100
29	Rn c	1.4	0.09L	0.006L	100
36	Rn d	1.4	0.10L	0.007L	100
56	Rn e	8.8	0.09L	0.06L	100
72	Rg 1	6.5	0.49L	-	1
			0.34L	-	1
			0.15L	-	3
			0.08L	-	12

346   The generation method presented above resulted in a maximum possible V_f of 56 %. In an effort to

347   generate explicit geometries at larger V_f, a regularly packed geometry was also considered, model

348   Rg1, also shown in Table 2. Rg1 is illustrated in Figure 6 where spheres of four different radii were

349   arranged to fill the cubic space of side L to a V_f of 72 %. The particle radii shown in Table 2 (0.49L,

350   0.34L, 0.15L and 0.08L) were chosen to ensure there was no contact between any particles.

351
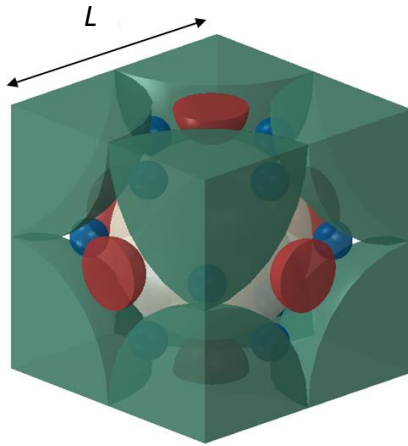
352   **Figure 6 Illustration of regular packed geometry for model Rg1.**

353   Table 3 shows the use of various combinations of the geometries summarised in Table 2 to achieve

354   predictions for different overall V_f. The latter is equal to the value shown last in each row of Table 3.

355   Each row corresponds to a different test case. Models labelled DM_XX are Scale *II* models where X

356   from a-e represents the geometries Rn a, Rn b, Rn c, Rn d and Rn e in Table 2 respectively. The

357   number of X characters therefore denotes the scale of the model. For example, Test case DM_dddd

358   is a scale *IV* model with Rn d passed hierarchically four times in itself as illustrated in Figure 5. The

359   resulting V_f at each scale leading to a final V_f of 83 % is presented in Table 3. The smallest and

360   largest volume fractions created were 21% (case DM_aa) and 83% (case DM_dddd) respectively. The

361   accuracy of the method was evaluated for the various scales by comparing predictions with those

362   obtained from explicitly packed FE models of the same filler V_f (i.e. scale *I*) up to 56 % for random

363   structures and 72% for the regular geometry (see Table 2).

364   The FE models outlined in Table 3 were meshed using quadratic tetrahedral elements (C3D10). The

365   implicit quasi-static algorithm in ABAQUS, (SIMULIA, Rhode Island) was employed. For the boundary

366   conditions, all surfaces were constrained to remain plane during deformation such that

367   homogeneous kinematic boundary conditions are implied. Displacement controlled tensile loading

368   up to an arbitrary level of 0.04 strain was applied to the top surface and a symmetry boundary

369   condition was applied to the opposite, bottom surface.

370   The average stress and strain were determined to define the bulk stress-strain response of the

371   composite using the surface integral method (Qin and Yang, 2008): stress was calculated by

372   summing the vertical reaction forces on all nodes on the top surface of the model divided by the

373   area of the top surface, whilst strain was evaluated using the applied displacement at the top

374   surface and the original height of the model. The elastic properties of the bulk homogenised

375   composite corresponding to the various models were determined using the stress and strain

376   response predicted by FE in the initial stages where energy dissipated by plasticity was zero. The

377   initial slope was used to define the composite modulus and the composite's Poisson's ratio was

378   determined using the lateral contraction of the RVE during tension. A proof stress of 0.002 plastic

379   strain was used to determine the yield stress, σ_Y^C, and yield strain, ε_Y^C. A mesh convergence study

380   was performed for all models. Mesh convergence was achieved, where insignificant change was

381   observed in the predicted elastic modulus and yield stress with increasing number of elements.

382

383

384

385

386

387

388

389

390

391

392

393

394

395

396

Table 3 Summary of multi-scale models for volume fractions ranging from 29% to 83%.

| Case	Symbol	Scale I	Scale II		Scale III		Scale IV	
		$\emptyset_I\%$	$\emptyset_{II}\%$	$V_{f_{II}}\%$	$\emptyset_{III}\%$	$V_{f_{III}}\%$	$\emptyset_{IV}\%$	$V_{f_{IV}}\%$
DM_aa	●	11	11	21	-	-	-	-
DM_aaa	▲	11	11	21	11	29	-	-
DM_aaaa	■	11	11	21	11	29	11	37
DM_aaab	■	11	11	21	11	29	19	43
DM_aaac	■	11	11	21	11	29	29	50
DM_aaad	■	11	11	21	11	29	36	55
DM_aab	▲	11	11	21	19	36	-	-
DM_aac	▲	11	11	21	29	44	-	-
DM_aad	▲	11	11	21	36	49	-	-
DM_ab	●	11	19	28	-	-	-	-
DM_aba	▲	11	19	28	11	36	-	-
DM_abb	▲	11	19	28	19	42	-	-
DM_abc	▲	11	19	28	29	49	-	-
DM_abd	▲	11	19	28	36	54	-	-
DM_ac	●	11	29	37	-	-	-	-
DM_ad	●	11	36	43	-	-	-	-
DM_ae	●	11	56	61	-	-	-	-
DM_ba	●	19	11	28	-	-	-	-
DM_bb	●	19	19	35	-	-	-	-
DM_bc	●	19	29	43	-	-	-	-
DM_bd	●	19	36	48	-	-	-	-
DM_be	●	19	56	65	-	-	-	-
DM_ca	●	29	11	37	-	-	-	-
DM_cb	●	29	19	43	-	-	-	-
DM_cc	●	29	29	50	-	-	-	-
DM_cd	●	29	36	55	-	-	-	-
DM_ce	●	29	56	69	-	-	-	-
DM_da	●	36	11	43	-	-	-	-
DM_db	●	36	19	48	-	-	-	-
DM_dc	●	36	29	55	-	-	-	-
DM_dd	●	36	36	59	-	-	-	-
DM_dda	▲	36	36	59	11	64	-	-
DM_ddb	▲	36	36	59	19	67	-	-
DM_ddc	▲	36	36	59	29	71	-	-
DM_ddd	▲	36	36	59	36	74	-	-
DM_ddda	■	36	36	59	36	74	11	77
DM_dddb	■	36	36	59	36	74	19	79
DM_dddc	■	36	36	59	36	74	29	82
DM_dddd	■	36	36	59	36	74	36	83
DM_de	●	36	56	72	-	-	-	-
DM_ea	●	56	11	61	-	-	-	-
DM_eb	●	56	19	65	-	-	-	-
DM_ec	●	56	29	69	-	-	-	-
DM_ed	●	56	36	72	-	-	-	-
DM_ee	●	56	56	81	-	-	-	-

6.0 Analytical models

The predictions from the finite element models described in section 5.0 were compared to composite elastic moduli at different V_f obtained from the Mori-Tanaka (MT) analytical model (Mori and Tanaka, 1973) extended for elastic- perfectly-plastic polymeric matrix particulate composite materials by Lin et al. (Lin et al., 1992). This analytical model was selected as the resulting equations are quick, easy to use and do not require iterative numerical solutions. Details of how this model was adopted for our study are given in the Appendix.

For the elastic modulus, several other models are reported in the literature (Stapountzi et al., 2009, Hagan et al., 2011); specifically, the original upper and lower bound models by Voigt and Reuss (Reuss, 1929; Voigt, 1889) as well as the refined bounds by Hashin-Shritkman (HS) (Hashin and Shtrikman, 1963) and Lielens (Lielens et al., 1998) were employed in this study for comparison with the composite modulus numerical predictions.

7.0 Numerical model results

7.1 Results for explicit finite element models

The five random models shown in Table 2 were first run explicitly (without the hierarchical multi-scale procedure) in order to compare the FE predictions with the analytical results from the elastic – plastic matrix model summarised in section 6. The latter was found to predict the E^c accurately for V_f up to 36 % (see Figure 7). However, at a V_f of 56 %, the E^c was underpredicted by 22 %. This is due to the increasing effect of the interaction between the particles, which is not captured correctly in the elastic plastic extension of the MT model (Lin et al, 1992). Significant error was found in the prediction of plastic behaviour. The FE solution diverges from the analytical solutions at the early stages of the linear region. This is because the onset of plasticity in the matrix volume is a progressive process in the FE models. Yielding first initiates locally in a region of matrix with high stress concentrations and the plastic zone grows with increasing deformation. In contrast, the bi-linear analytical model assumes the entire matrix volume behaves linearly until the matrix yield stress is reached; at this point, the entire matrix volume behaves plastically. The sharp transition between the elastic and plastic phase leads to an overprediction of the composite yield stress, σ_Y^c, with the error increasing from 15 % at a V_f of 10.9 % to 26 % at a V_f of 56.3 %. Yield strain, ε_Y^c was determined from the σ_Y^c and the E^c and the agreement of the solutions are dependent on those for the other two properties with the largest error being 17 % at a V_f of 56.3 % (results not shown).
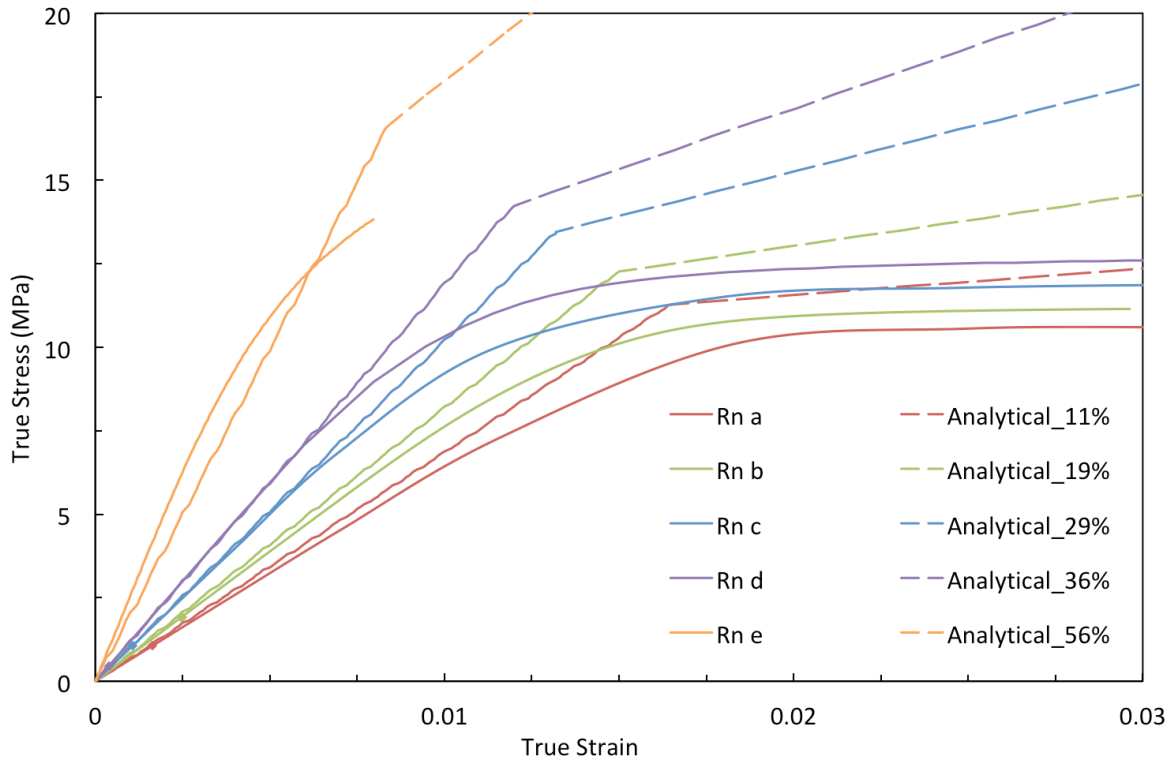
Figure 7 Comparison of the composite stress-strain curve predicted from the Mori-Tanaka model extended to elastic-plastic matrix composites (see Appendix) and explicit (scale *I*) finite element models for five different filler volume fractions (Models Rn a – Rn e as shown in Table 2).

The elastic Poisson's ratio determined using the rule of mixtures (equation A6 in Appendix) was found to agree with those obtained from FE, with errors ranging between 0.5-4 % (data not shown).

The results from this part of the study show that the use of the elastic plastic extension of the MT model (Lin et al , 1992) to account for the missing fine particles embedded in an elastic-plastic matrix is inaccurate and could lead to significant errors in the predicted behaviour of highly filled composites. This further highlights the need the decoupled multi-scale FE models described in section 5 whose results are next presented.

7.2 Results for decoupled multi-scale finite element models

This section presents the results from the hierarchical multi-scale models described in section 5.0, as summarised in Table 3. The values of E^c, v^c, σ_Y^c and ε_Y^c determined from the homogenised stress-strain curves are plotted in Figures 8 -11 respectively as a function of V_f. For Figures 9 - 11, the results predicted by the MT analytical model extended to elastic – plastic matrix (see Appendix) are

447 shown, as are the predictions from the explicit scale I models up to a maximum of 56 % (see 'Explicit'

448 curves). The range of explicit models was extended to 72 % through the use of the regular body

449 centre cubic RVE, Rg1, shown in Figure 6 and Table 2. For the elastic modulus (Figure 8), the results

450 are also compared to the Voigt, Reuss and Hashin-Shritkman (H-S) bounds as well as the Lielens

451 model. Note that the symbols used to plot the data from the hierarchical multi scale models in

452 Figures 8 – 11 correspond to the symbols shown in the second column of Table 3 (for example the

453 data points DM_aX in Figures 8-11, correspond to the data derived from the models DM_aa, DM_ab,

454 DM_ac, DM_ad and DM_ae listed in Table 3, all labelled with the same symbol).

455 The first point to note is that in all of Figures 8 – 11, the elastic and plastic properties derived by all

456 simulations summarised in Table 3 fall on roughly the same curve. Now for the elastic properties

457 (Figures 8-9), the results are as expected as it is known that for a given matrix-particle combination,

458 only the volume fraction and aspect ratio affect the bulk behaviour. But the fact that plastic

459 properties also fall on the same curve, is evidence that the hierarchical multi-scale model leads to

460 consistent predictions, giving confidence in the accuracy of the method. It also highlights that the

461 exact particle size distribution does not have a significant effect on the onset of plasticity in the

462 composite (see various distributions assumed in the explicit models in Table 2). The difference

463 between the various curves in Figures 8-11 is difficult to see in the plots and is described in more

464 detail below.

465 The values of E^c (see Figure 8) and ν^c (see Figure 9) increase and decrease respectively as V_f

466 increases as expected. In Figure 8, E^c values fall within the upper and lower bounds derived using

467 the analytical models detailed in section 6, with the best agreement shown to the Lielens model. The

468 latter has also been found to be the most accurate analytical model in other studies involving

469 experimental data of polymeric matrix composites (Stapountzi et al 2009, Hagan et al 2011). For V_f

470 up to 56 %, E^c and ν^c predicted at scale II (DM_aX, DM_bX, DM_cX, DM_dx, DM_eX) using the

471 hierarchical method were found to be within 10 % and 5 % respectively of those predicted using the

472 explicit method (scale I) and a maximum error of 16 % and 6 % respectively compared to the elastic-

473 plastic MT model (see Appendix) predictions. For scale III (DM_aaX, DM_abX and DM_ddX), the

474 maximum errors for all cases increased to 13 % and 6 % respectively compared to the explicit models

475 and 35 % and 10 % respectively compared to the elastic-plastic MT model predictions. Finally, for

476 scale IV (DM_aaaX, DM_dddX), the maximum errors were 17 % and 7 % respectively compared to

477 the scale I models and 25 % and 11 % respectively compared to the elastic-plastic MT model

478 predictions. In addition, the elastic properties derived from the Rg1 model (see Table 2) were found

479 to be within 4 % of the hierarchical model predictions. The prediction of ν^c from the multi-scale

480 models was found to be higher than those predicted using equation A6 (see Figure 9). This is

481 because the lateral contraction becomes increasingly constricted due to the pinning of filler particles

482 by each other, thereby resulting in a lower compressibility than that predicted by the analytical

483 models.

484 In Figures 10 and 11, predictions for the σ_Y^C and ε_Y^C below a V_f of 56 % from the scale II and scale III

485 models were found to be within 8 % and 7 % of the explicit scale I model predictions. The

486 predictions above 56 % (highest volume fraction of explicit random models in Table 2) appear to

487 follow the same trend of the σ_Y^C that would be expected from extrapolation of the data and

488 increased nonlinearly with V_f. Similar to that observed for the explicit scale I and Rg1 FE solutions

489 (see Figure 7), the hierarchical model predictions for σ_Y^C were lower than those predicted by the

490 elastic – plastic MT model (see Figure 10). It is also worth noting that the omission of finer particles

491 and the homogenisation of the entire 'matrix' volume at the larger length scales essentially increases

492 the volume of material that can undergo plasticity and decreases the volume of the elastic material.

493 Additionally, it was feared that this could result in a lower plateau stress and affect the accuracy of

494 the behaviour predicted in the plastic region. However, only a 2.5 % error was observed between

495 the hierarchical and scale I plateau stress predictions for a filler V_f of 29 %, a 3.9 % error for $V_f =$

496 36 % and a 8 % error for $V_f = 56$ %.

497 The predicted behaviour for the same V_f using different combinations of explicit filler ϕ_n were also

498 compared. For example, a prediction for a V_f of 69 % could be obtained by incorporating

499 homogenised material properties for a ϕ_I of 29 % into an explicit FE model of $\phi_{II} = 56$ % (see test

500 case DM_ce in Table 3). Alternatively, the same V_f of 69 % could also be reached by incorporating a

501 homogenised ϕ_I of 56 % into an explicit FE model of $\phi_{II} = 29$ % (test case DM_ec in Table 3). A

502 higher recoverable strain energy was expected in test case DM_ce due to larger amount of elastic

503 fillers modelled explicitly. However, the magnitude of the recoverable strain energy is insignificant in

504 comparison to the energy dissipated due to plasticity in the matrix. As a result, little difference was

505 observed in the total internal energies and consequentially the elastic and plastic properties of the

506 respective volumes were similar as shown in Figures 8-11.

507 Lastly, it is worth noting that the hierarchical model discussed above assumed a rate independent,

508 perfectly plastic binder material in order to simplify the study. In future, the approach should also be

509 validated for rate dependent, strain hardening binders such as those used in PBX. Here we will

510 assume the approach would hold for such more complex binders and we will extend to the PBX case

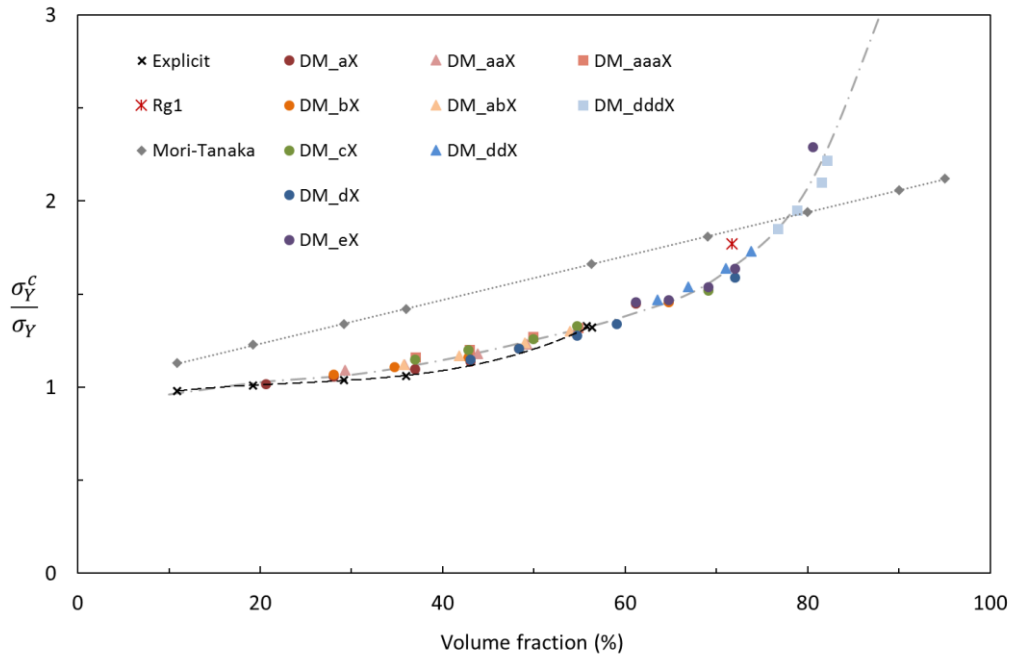511 in a manner described in the following section.

512

513
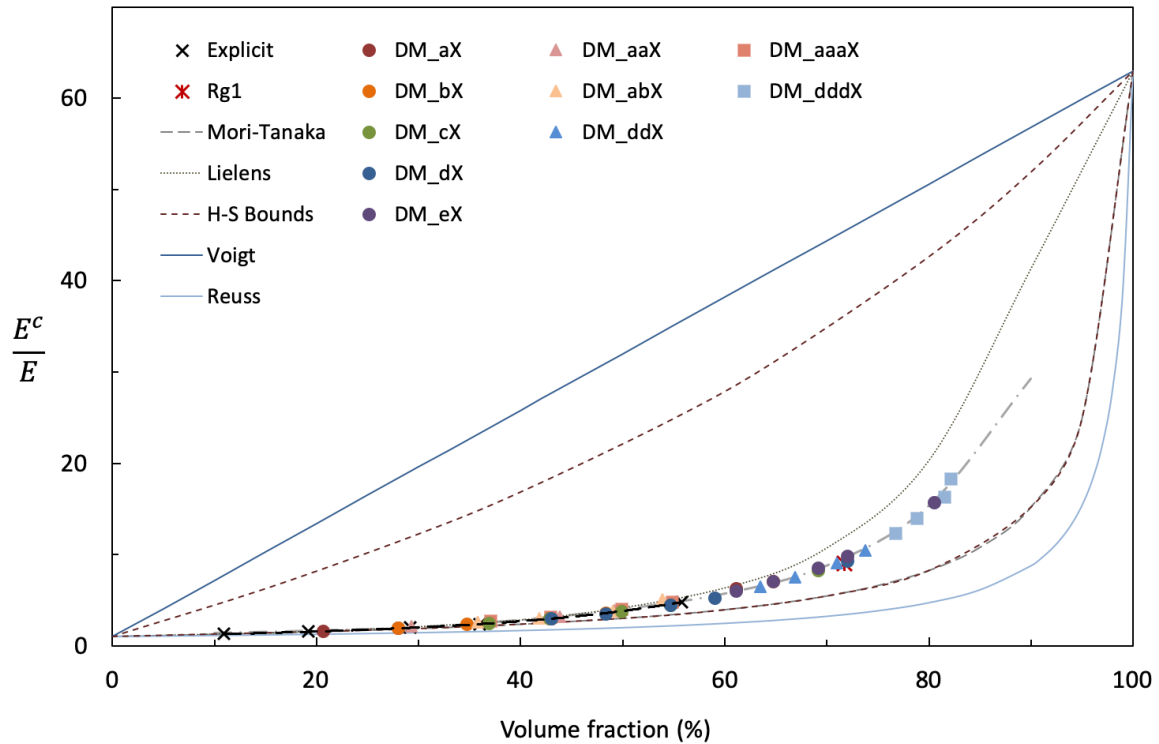
Figure 8 Hierarchical model predictions for $\frac{E^c}{E}$. The Explicit series includes the models Rn a, Rn b, Rn c, Rn d and Rn e. X denotes the letters a-e for the DM data series (see table 3) and the trend line for the DM data series is plotted in grey by a (dot-dash) line. Trend line for the explicit series is shown by the black dash line. The analytical models (Mori-Tanaka, Lielens, H-S Bounds, Voight and Reuss models) are discussed in Section 6.0.
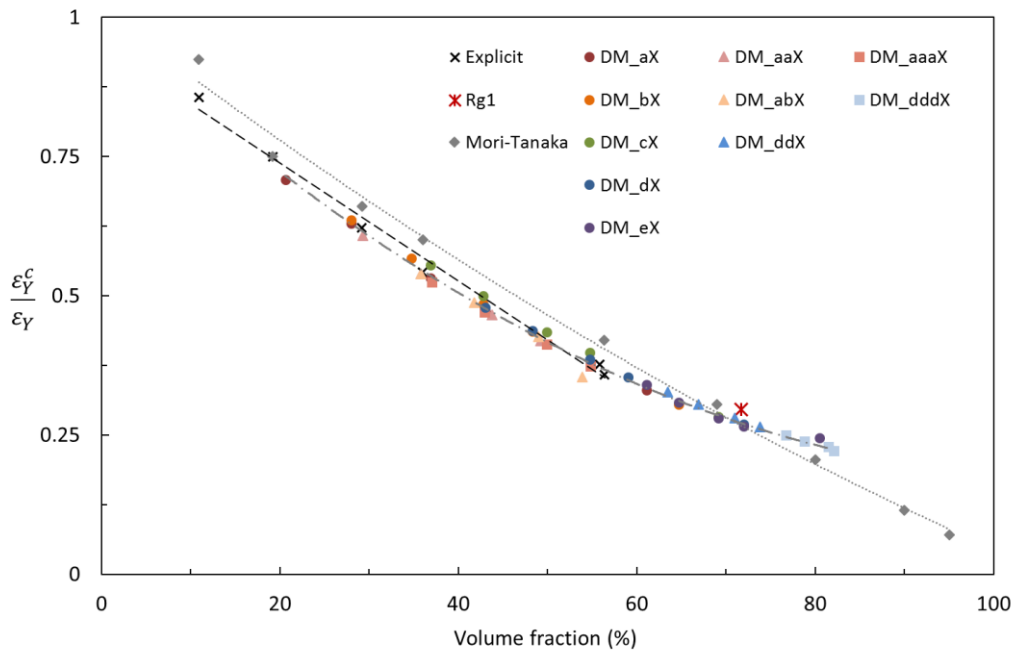

519
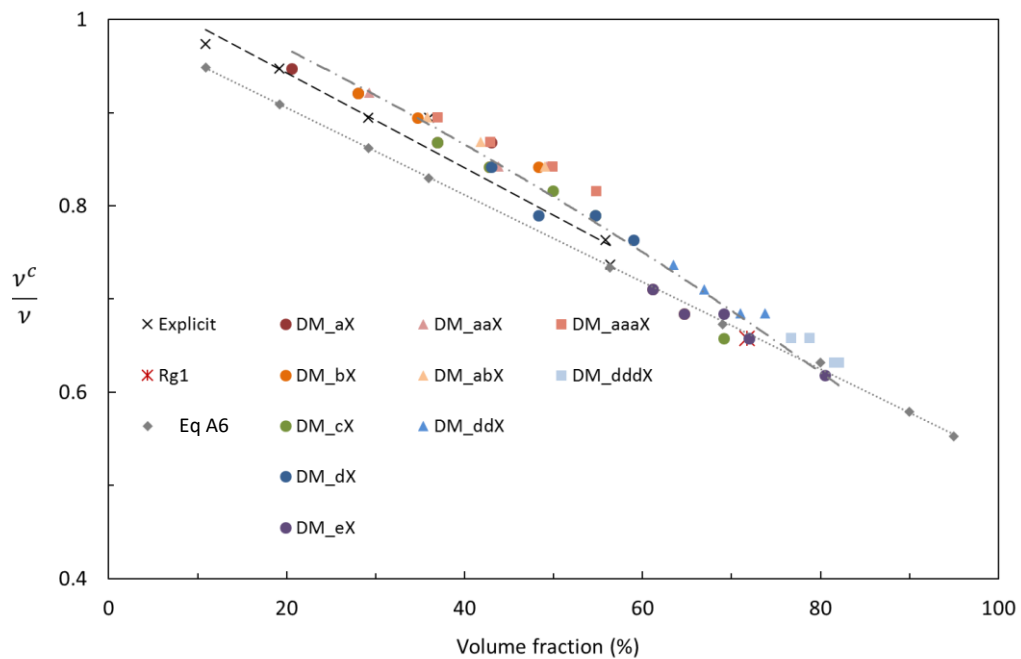
Figure 9 Hierarchical model predictions for $\frac{v_C}{v}$. The Explicit series includes the models Rn a, Rn b, Rn c, Rn d and Rn e. X denotes the letters a-e for the DM data series (see table 3). The trend line for the DM data series is plotted in grey by a (dot-dash) line and the Trend line for the explicit series is shown by the black dash line.

Figure 10 Hierarchical model predictions for $\frac{\sigma_Y^c}{\sigma_Y}$. The Explicit series includes the models the models Rn a, Rn b, Rn c, Rn d and Rn e. X denotes the letters a-e for the DM data series (see table 3) and the trend line for the DM data series is the grey (dot-dash) line. The trend line for the explicit series is shown by the black dash line. The Mori-Tanka model refers to the model described in the Appendix.
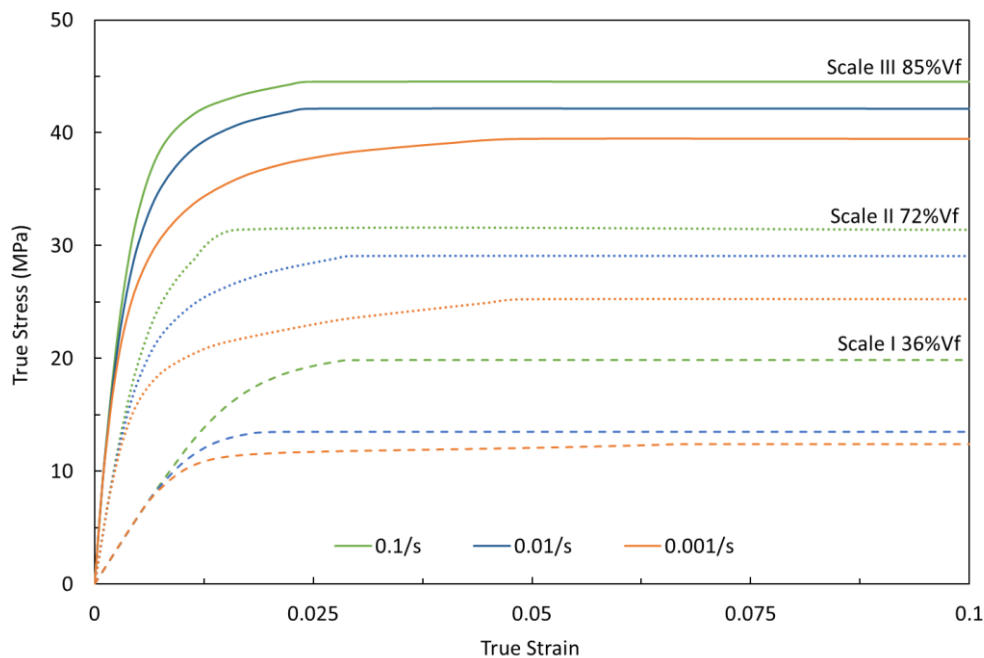

Figure 11 Hierarchical model predictions for $\frac{\varepsilon_Y^c}{\varepsilon_Y}$. The Explicit series includes the models the models Rn a, Rn b, Rn c, Rn d and Rn e. X denotes the letters a-e for the DM data series (see table 3) and the trend line for the DM data series is the grey (dot-dash) line. The trend line for the explicit series is shown by the black dash line. The Mori-Tanka model refers to the model described in the Appendix.

7.3 Use of the multi-scale method for predicting the PBX composite behaviour

Here the results of the models described in section 4 are presented. With the VEs of V_f = 65-72 % shown in Figure 2 used to model the PBX composite of a total V_f = 95 % , a V_f of 23-30 % with respect to the whole composite volume is lost in the matrix material. Thus, homogenised behaviour of a sub-volume with a V_f of 82-86 % is required such that for the 65% particles explicitly modelled there is 0.65 + 0.86 (1 - 0.65) = 0.95 which is the required filler content. A scale *III* hierarchical model was used to predict the homogenised behaviour, with $\phi_I = 36$ %, $\phi_{II} = 56$ % and $\phi_{III} = 45$ %, resulting in $V_{f_{III}} = 85$ % (see equation 5). An elasto-viscoplastic matrix model is assumed for the scale *I* model with strain hardening where Young's modulus, $E = 500$ MPa, Poisson's ratio, $v = 0.38$ and rate dependent yield stresses, $\sigma_Y(\dot{\varepsilon} = 0.0014) = 9.15$ MPa and $\sigma_Y(\dot{\varepsilon} = 0.14) = 16.6$ MPa as already described in section 2.1. This model fit to the FK800 experimental data is shown in Figure 1(b). As the matrix material is elastic-viscoplastic, homogenisation at each scale was performed at three different strain rates, 0.001, 0.01 and 0.1 /s and the predicted homogenised parameters, E, v and $\sigma_Y(\dot{\varepsilon})$, where $\dot{\varepsilon} = 0.001 /s, 0.01 /s$ and $0.1 /s$ were sequentially substituted into the matrix properties of the next scale model. The homogenised elastic-viscoplastic behaviour predicted using the hierarchical models at a V_f of 36 % (scale *I*), 72 % (scale *II*) and the final V_f of 85 % (scale *III*) are shown in Figure 12. The resulting elastic-viscoplastic behaviour predicted for a V_f of 85 % was used to define the matrix properties of the 2D micromechanical model described in section 4.0.

Figure 12 Homogenised stress-strain predictions at different volume fractions using the multi-scale hierarchical model.

559 The randomly packed microstructure leads to a non-uniform inter-particle spacing. Regions with

560 smaller inter-particle spacing and a lower matrix volume experience much higher localised strains

561 and strain rates than that applied to the bulk material. It was therefore essential to ensure that at

562 each scale, the matrix material model was calibrated to a strain and strain rate sufficient to allow for

563 the highest local strain and strain rate anticipated. The ratio between the highest strain experienced

564 in the model and the applied strain was found to be 10 for $\phi_I = 36$ %, 20 for $\phi_{II} = 56$ % and 15 for

565 $\phi_{III} = 45$ %. The same ratios were also found between the highest strain rate experienced and the

566 strain rate applied. Consequently, to model the composite with a strain of 0.0025 applied at a strain

567 rate of 0.00005 /s (see section 4.0), mechanical data for $\varepsilon_{max} = 7.5$ (equal to 10x20x15x0.0025) and

568 $\dot{\varepsilon}_{max} = 0.15$ /s were required for the matrix material calibration. However, as shown in Figure 1(b)

569 the matrix material fractures at $\varepsilon(0.14$ /s) = 1.2 and $\varepsilon(0.0014$ /s) = 1.4. In the current model, strain

570 hardening was therefore described up to $\varepsilon = 1.2$ beyond which the matrix was assumed to behave

571 perfectly plastically. It is recommended that in future models, matrix fracture and damage occurring

572 at larger strains should also be implemented in the model. The highest strain rate at which

573 mechanical data for the matrix material is available is 0.14 /s. As the required maximum strain rate

574 was estimated to be 0.15 /s, calibration of the material model with $\dot{\varepsilon}_{max} = 0.14$ /s was assumed to

575 be sufficient. The minimum strain rate required for the model calibration was estimated to be

576 0.00001 /s, two decades lower than the slowest strain rate available of 0.0014 /s. However, only 2%

577 of the matrix material was predicted to experience a strain rate less than the applied strain rate of

578 0.00005 /s.

579

580 **7.3.1 Comparisons to experimental data**

581 Figure 13 shows the composite tensile behaviour determined using the 2D FE model corresponding

582 to the four VEs of Figure 2. A good agreement was found between the four models in both the

583 modulus and the onset of catastrophic failure, giving confidence to our results and the choice of the

584 microstructural images shown in Figure 2 as volume elements. The model data beyond the onset of

585 failure are not shown; this is because the binder's constitutive response did not implement a

586 damage model and as a result the binder would stretch indefinitely which is of course not

587 representative of the real response where the matrix will tear, and force will drop to zero. The

588 predictions were compared to the experimental data, also shown in Figure 13. The initial response

589 predicted by the FE model was found to be overly stiff with an average $E^c = 19.5$ GPa in

590 comparison to the range measured experimentally where 6.5 GPa $< E^c <$ 11.6 GPa . The failure

591 strain was under-predicted where an average of $\varepsilon_Y^c = 0.00061$ was obtained by FE and $\varepsilon_Y^c =$

592 0.0017 was measured experimentally. The average fracture stress was estimated to be 11.3 MPa

593 from the four VEs in comparison to an average of 8.2 MPa measured experimentally.

594

595
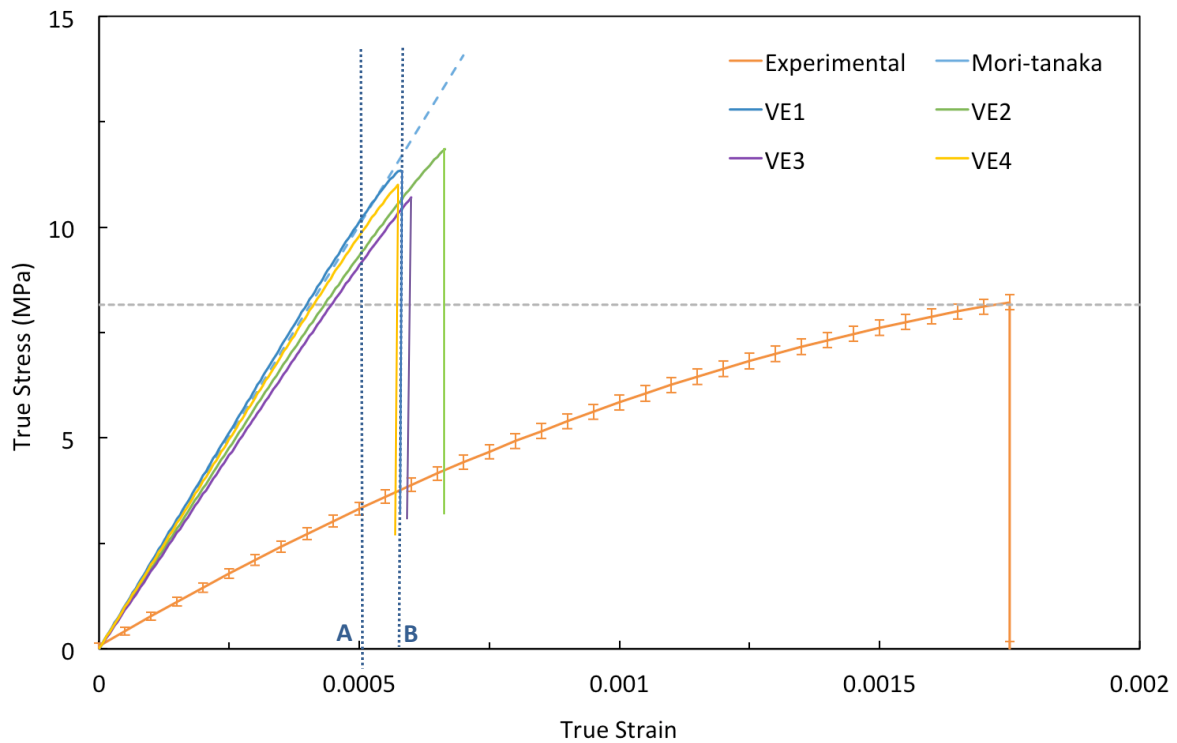
Figure 13 Composite tensile behaviour measured experimentally and predicted using finite element models (using four VEs in Figure 2) as well as analytically (Mori-Tanaka). Points A and B marked with blue dotted lines correspond to the points prior to and at the onset of catastrophic failure for VE1.

600

601 In order to investigate the discrepancy, the modulus of a 95 % filled TATB/FK800 as calculated using

602 the MT and Lielens models was considered (see Figure 8). The latter gave values of 11 GPa and 26

603 GPa which are close to the numerical modulus of 19.5 GPa, and both considerably higher than the

604 experimentally derived modulus. In fact, the experimentally determined average value of the

605 composite modulus $E^c = 8.6$ GPa and the matrix modulus $= 500$ MPa , lead to a ratio $E^c/E = 17.2$.

606 From Figure 8, at 95% volume fraction, this value is extremely low and falls even lower than the

607 lower bound of the H-S model, close to the Reuss model (Saeb et al., 2016). The latter is known to be

608 unrealistically low. Therefore, possible reasons for why the PBX composite behaved in a more

609 compliant manner than would be expected were next considered. Uniaxial tensile tests were

610 performed on annealed binder materials. Samples were heated to 120 °C in a press at 5 tonnes for

611 three minutes. The press was then water cooled with samples still under pressure until the

612 temperature of 30 °C was reached at which time the pressure was released and the samples were

613   removed. Samples were then cut to size and tested at the rate of 0.0014 /s (see Figure 14). The

614   results showed that the heating and cooling of the binder results in an amorphous, more compliant

615   polymer that did not display the typical strain softening and hardening behaviour of semi-crystalline

616   polymers as seen in Figure 1(b). The modulus of the annealed polymer is in fact about 50% lower

617   than the previously tested, untreated samples. Using a matrix value of 250 MPa instead of the

618   previous value of 500 MPa would bring the analytical modulus calculations down to 7.5 GPa and 23

619   GPa for MT and Lielens models respectively. Therefore, it is believed that the observed discrepancy

620   could be at least partly due to a change in the binder material properties during the hot isostatic

621   pressing of the composite. The high V_f of rigid fillers may impede the re-organisation of the polymer

622   chains and result in a lower crystallinity polymer compared to the unprocessed binder used in the

623   characterisation of the matrix. Furthermore, another reason for the disagreement between the

624   predicted modulus and the experimental data could be due to the 2D plane strain assumption made

625   in the FE models. This is known to lead to an overly stiff response as compared to full 3D simulations

626   with a reported overestimation of modulus and fracture strength of approximately 28% and 15%

627   respectively (Arora et al, 2015). Running 3D simulations of such complex microstructures is a real

628   challenge however, both in terms of the required computational resource as well as acquiring

629   suitable 3D images in the first place through microstructural characterisation experiments. Lastly, in

630   the real composite, microcracks could have formed in the material during the manufacturing

631   stresses or due to residual stresses arising during the cooling stage after pressing; such cracks could

632   also lower the modulus and strength of the composite.

633   Next, the numerical models were used to examine the damage process and failure mode of the PBX.

634   The points prior to and at the onset of catastrophic failure for VE1 are marked in Figure 13 and are

635   labelled points A and B respectively. Equivalent points were defined for the rest of the VE's in a

636   similar fashion. The total energies dissipated due to plastic deformation and interfacial debonding

637   for VE1 are shown in Figure 15 as a function of the applied strain. In addition, contour plots of the

638   cohesive elements' degradation factor are presented in Figure 16 corresponding to points A and B

639   for all four VE's. A degradation factor of 0 (i.e. prior and at damage initiation) is indicated in blue

640   colour and maximum degradation factor of 1 (i.e. debonding occurs and the cohesive element's

641   stiffness is reduced to zero) is indicated in red colour.

642
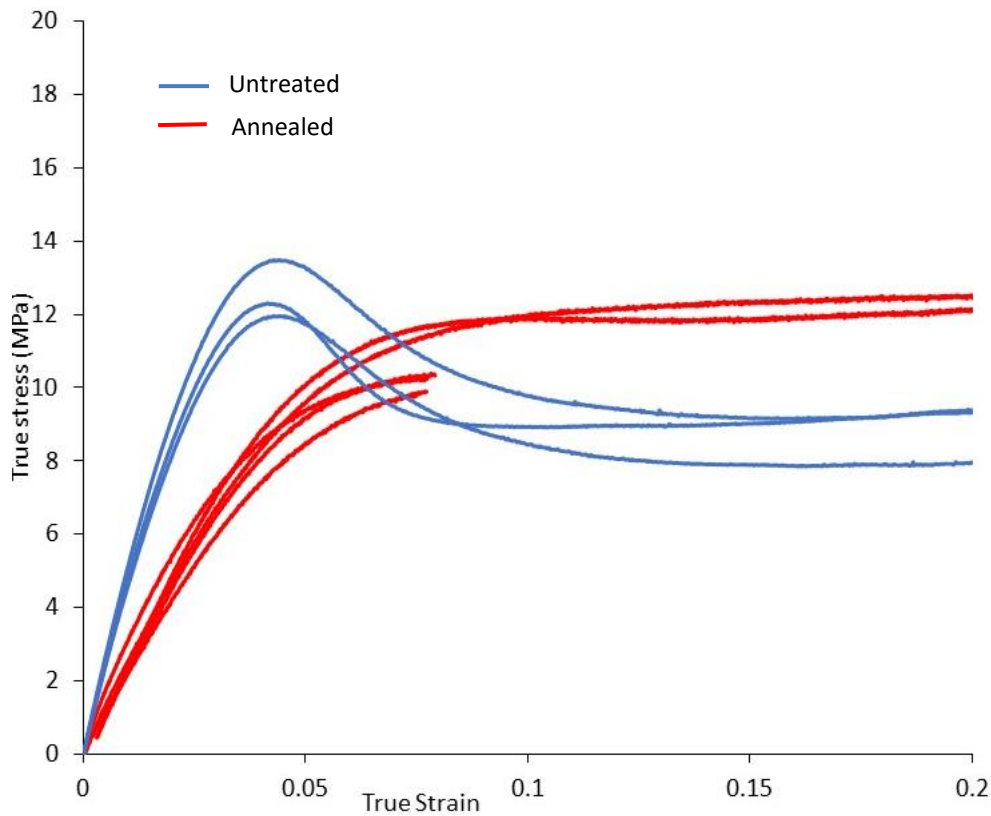
Figure 14: Comparison of stress-strain curves from annealed and original (untreated, see Figure 1(b)) samples tested at 0.0014 /s rate.

In Figure 15, an initial region between points A and B is observed where the energy dissipated due to plasticity and debonding is slowly rising with strain. In this region, a comparable amount of energy was dissipated by both mechanisms and it was therefore concluded that the small non-linearity in Figure 13 before the step drop in stress is due to both initiation of filler-matrix interface failure (i.e. degradation of the cohesive elements) and plastic yielding of the matrix material. At the point of failure, point B, the energy dissipated sharply increases which corresponded with the first sudden stress drop in Figure 13. The energy dissipation is now predominantly due to debonding around the fillers. The debonding at point B is also evident in Figure 16 in subplots B1-B4. At this point, which is the maximum tensile strength of the composite, multiple filler debonding occurs, debonding becomes the dominant mode for energy dissipation and catastrophic failure takes place. It is worth noting here that as shown in Figure 16, debonding was observed to first initiate around the larger particles and those that have straight edges aligned normal to the tensile load direction in agreement with previous research (Rae et al., 2002, Arora et al, 2015).

Finally, it is worth noting that although the applied bulk strain of 0.0025 is a great deal lower than the yield strains of the matrix which are $\varepsilon_Y(0.0014) = 0.018$ and $\varepsilon_Y(0.14) = 0.033$ from Figure 1(b), observations from the FE models showed that the matrix region within the composite

662 experiences a significant amount of plasticity. Thus, the viscoplastic constitutive model is essential

663 for accurate prediction of the highly filled composite behaviour, even when failure occurs at small

664 applied strains.
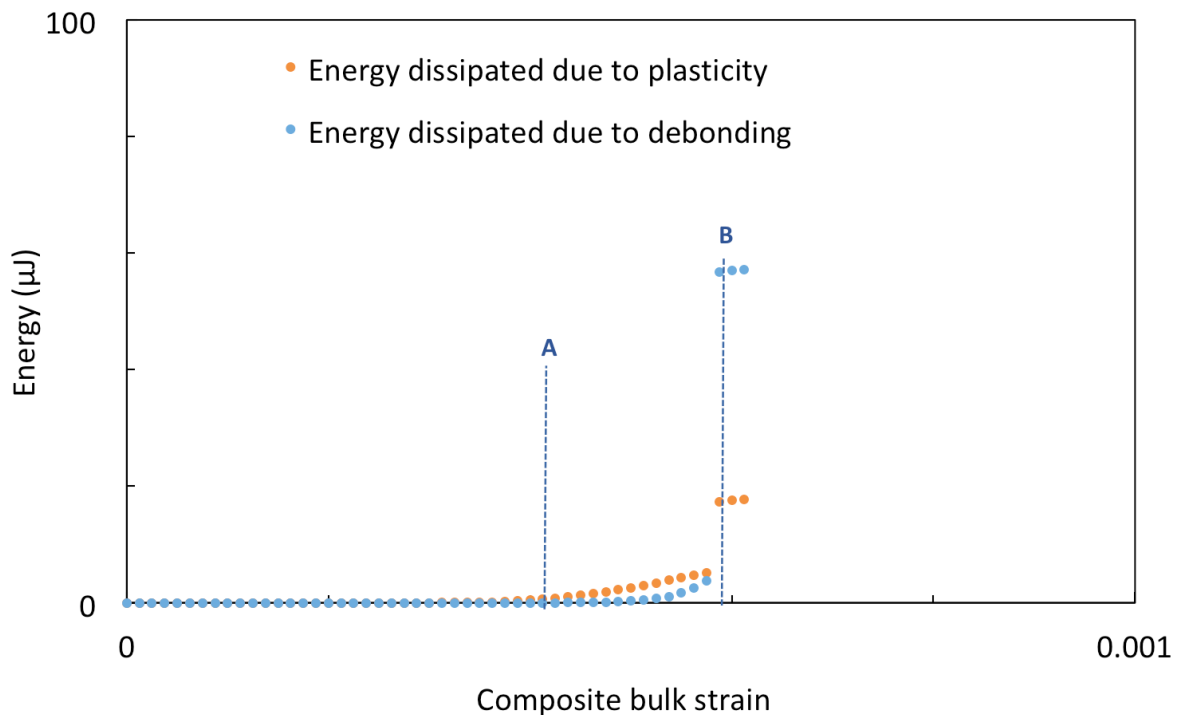
665 **Figure 15 Energy dissipation by interface debonding and matrix yielding as a function of applied**
666 **strain for VE1 in Figure 2; the other three VE's shown in Figure 2 led to similar behaviour (results**
667 **not shown).**
668

669 In summary, the recommendations arising from the presented study are as follows: when the

670 reinforcing particles in composites appear at multiple length scales, micromechanical models which

671 consider all particles explicitly are often deemed unfeasible. In such cases, hierarchical multi-scale

672 models where the smaller particles are implicitly accounted for through reinforcing the matrix in

673 nested, progressively higher scale models are viable (see Figure 5) and provide accurate predictions

674 of the homogenised composite. In this study, this approach was followed for a high performance

675 energetic material in the following manner: real microstructure images were processed and fed into

676 finite element models were the larger particles were explicitly modelled as they appear in the

677 images. The smaller, 'lost' particles were modelled implicitly through the hierarchical multi-scale

678 model, by assigning the matrix properties to be that of the binder reinforced with these smaller

679 particles. The models proposed in this study offer novel design tools for predicting the mechanical

680 response of high volume fraction particulate composites such as PBX materials. The method is

681   generic and can be applied to other composite materials; it may be easily modified to allow for other

682   failure mechanisms such as damage in the matrix and/or the fillers. Extensive multi-scale simulations

683   are however required for the homogenised matrix of the PBX material consisting of binder and the

684   implicitly modelled smaller particles; this ought to be considered when making choices between

685   simpler, phenomenological models or fundamental, mechanistic approaches such as the ones

686   presented here.

687
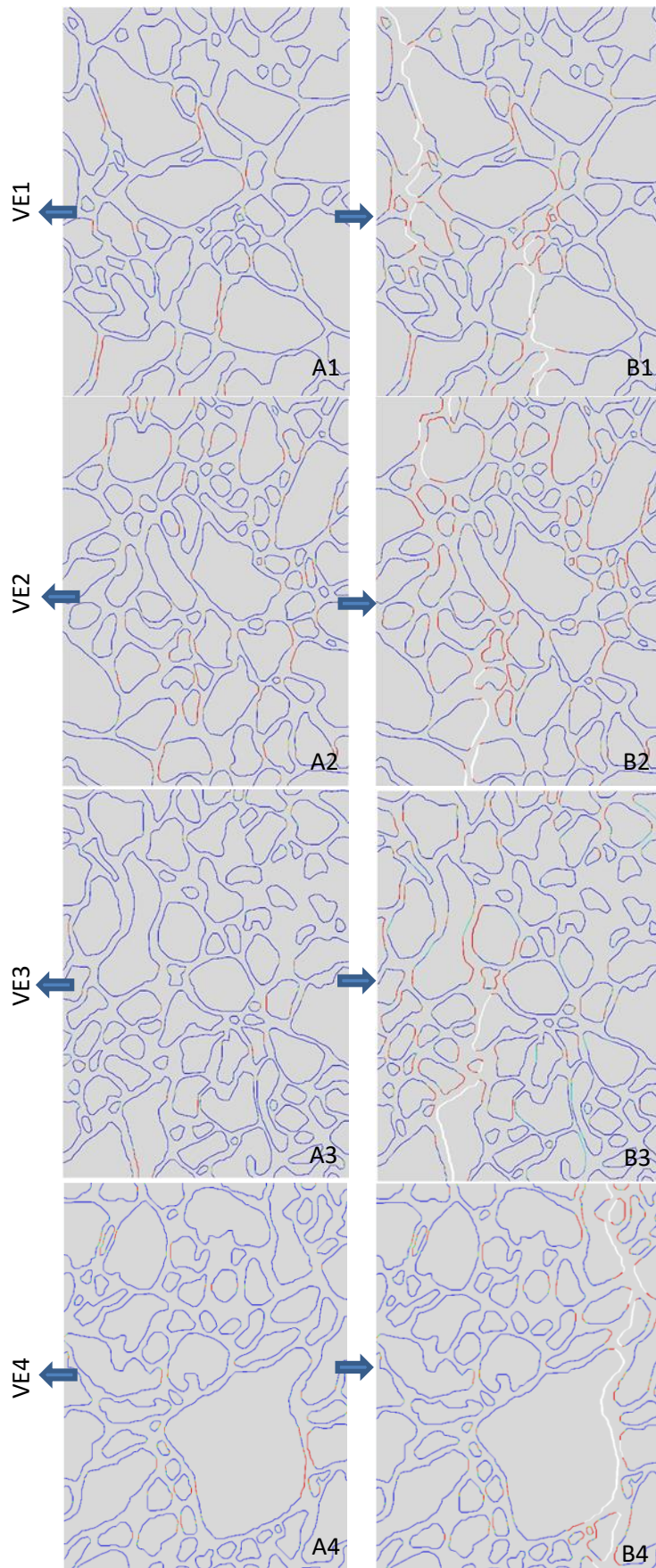
Figure 16 Progressive cohesive failure before (A1-A4) and at onset of catastrophic failure (B1-B4) predicted by the four VEs of Figure 2 corresponding to points A and B in Figure 13. Arrows show direction of applied load. Blue indicates interfaces not actively debonding, red indicates interfaces

691 **actively debonding and the white spaces are openings where the interface has failed and is fully**
692 **debonded.**

693

694 **8.0 Conclusions**

695 A novel hierarchical multi-scale model was developed, suitable for extremely high-volume fraction

696 particulate composites. The predictions of the elastic-plastic properties of the composite were found

697 to be in close agreement with explicit model results. The hierarchical modelling method was applied

698 to a polymer bonded explosive of a 95 % filler volume fraction with a viscoplastic binder and the

699 predicted composite stress-strain behaviour was compared to uniaxial tensile test data. Volume

700 Elements were reconstructed from Focussed Ion Beam scan data of the composite and fracture

701 stresses predicted by the four VEs used were found to be comparable to that measured

702 experimentally. The composite's behaviour predicted using the hierarchical finite element method

703 was found to be considerably stiffer than that determined from experimental data. Potential reasons

704 for the discrepancy are due to changes to the binder and specifically lower crystallinity during the

705 manufacturing process for the composites, the limitation of the assumed 2D plane strain model as

706 well as possible porosity in the composite not accounted for in the model. The novel hierarchical

707 multi-scale method presented here forms the basis from which a full 3D model may be developed,

708 leading to a powerful tool for predicting the mechanical behaviour of very highly filled viscoplastic

709 matrix particulate composites. The highly adaptable and versatile method has advantages over other

710 published methods as it allows the incorporation of arbitrary particle geometries, large particle size

711 distribution, non-linear matrix properties and complex matrix-filler interfacial properties.

712

713 **Appendix**

714 For a given particulate composite with an elasto-perfectly-plastic matrix and elastic spherical fillers

715 assumed not to yield within the stress range of interest, the characteristic behaviour of the material

716 can be approximated using a bilinear description (Lin et al., 1992). The first stage, stage 1, is the

717 region where both materials exhibit linear elastic behaviour. The overall average shear stress-strain

718 relationship,

719 $\tilde{\sigma}_{12,1}^{o} - \tilde{\varepsilon}_{12,1}$, during stage 1 is described by:

$$\tilde{\sigma}_{12,1}^{o} = 2\mu \left[1 - \frac{V_f(1-m)}{1 - (1-V_f)(1-m)\beta} \right] \tilde{\varepsilon}_{12,1} \qquad \text{[A1]}$$

720   where $\tilde{\sigma}^o_{12,1}$ and $\tilde{\varepsilon}_{12,1}$ are the bulk shear stress and shear strain of the composite during stage 1,

721     $m = \frac{\mu^*}{\mu}$, μ^* and μ are the shear moduli of the filler and matrix respectively, V_f is the filler volume

722   fraction and β is the deviatoric component of the decomposed Eshelby tensor. For spherical

723   inclusions, $\beta = \frac{2(4-5v)}{15(1-v)}$, and v is the Poisson's ratio of the matrix material.

724   This linear stress-strain relationship no longer holds when the stress in the matrix reaches the yield

725   stress of the matrix, τ_Y. By assuming there is negligible plasticity at the first instance yielding

726   initiates, the yield stress of the composite in shear, $(\tilde{\sigma}^o_{12})^c_Y$ can be determined by:

$$(\tilde{\sigma}^o_{12})^c_Y = \left[1 + \frac{V_f(\beta - 1)(1 - m)}{1 - \beta(1 - m)}\right]\tau_Y \qquad [A2]$$

727   The second stage, stage 2, describes the behaviour of the composite when the matrix material is

728   deforming plastically but the filler particles remain elastic. For an elastic-perfectly plastic matrix, the

729   stress experienced in the matrix material within the composite after yield is assumed to remain at

730   τ_Y. The bulk stress-strain relationship of the composite in stage 2, $\tilde{\sigma}^o_{12,2} - \tilde{\varepsilon}_{12,2}$, is then given by:

$$\tilde{\sigma}^o_{12,2} = 2\mu \frac{mV_f(1 - \beta)}{(1 - \beta) + m\beta(1 - V_f)}\tilde{\varepsilon}_{12,2} - \frac{(1 - V_f)[(1 - m)\beta - 1]}{(1 - \beta) + m\beta(1 - V_f)}\tau_Y \qquad [A3]$$

731   The shear and Young's moduli of the composite for the elastic stage 1 are here denoted as

732     $\mu^c_{,1}$ and $E^c_{,1}$, whereas the work hardening rate for stage 2 in shear and uniaxial deformation are

733   denoted as , $\mu^c_{,2}$ and $E^c_{,2}$. The four quantities are determined using equations A4 and A5:

$$\mu^c_{,n} = \frac{\tilde{\sigma}^o_{12,n}}{2\tilde{\varepsilon}_{12,n}} \qquad\qquad \text{where } n = 1, 2 \qquad [A4]$$

$$E^c_{,n} = 2\mu^c_{,n}(1 + v^c) \qquad\qquad \text{where } n = 1, 2 \qquad [A5]$$

734   where v and v^* are the Poisson's ratios of the matrix (here equal to 0.38) and filler (here 0.2)

735   respectively. The Poisson's ratio of the composite, $v^c_{,n}$, is predicted using the rule of mixtures, via

736   equations A6 and A7:

$$v^c_{,1} = v(1 - V_f) + v^*V_f \qquad\qquad \text{for } \tilde{\sigma}^o_{12} < (\tilde{\sigma}^o_{12})^c_Y \qquad [A6]$$

$$v^c_{,2} = 0.5(1 - V_f) + v^*V_f \qquad\qquad \text{for } \tilde{\sigma}^o_{12} > (\tilde{\sigma}^o_{12})^c_Y \qquad [A7]$$

737

738

739

750 **Data Availability**

751 The raw data required to reproduce these findings are available by contacting

752 soft.solids@imperial.ac.uk

753

754 **References**

755 Aboudi, J., Arnold, S.M., Bednarcyk, B.A., 2013. Multiscale Modelling of Composites, Micromechanics
756 of Composite Materials. Elsevier, pp. 447-540.
757 An, Q., Goddard, W.A., Zybin, S.V., Jaramillo-Botero, A., Zhou, T., 2013. Highly Shocked Polymer
758 Bonded Explosives at a Nonplanar Interface: Hot-Spot Formation Leading to Detonation. The Journal
759 of Physical Chemistry C 117, 26551-26561.
760 Annapragada, S.R., Sun, D., Garimella, S.V., 2007. Prediction of effective thermo-mechanical
761 properties of particulate composites. Computational Materials Science 40, 255-266.
762 Anoop, N.A., 2013. Energetic Polymers, Department of Applied Chemistry. Cochin University of
763 Science and Technology, p. 204.
764 Arora, H., Tarleton, E., Li-Mayer, J., Charalambides, M.N., Lewis, D., 2015. Modelling the damage and
765 deformation process in a plastic bonded explosive microstructure under tension using the finite
766 element method. Computational Materials Science 110, 91-101.
767 Baer, M.R., 2002. Modeling heterogeneous energetic materials at the mesoscale. Thermochimica
768 Acta 384, 351-367.
769 Bailey, A., Bellerby, J.M., Kinloch, S.A., Sharma, J., Baughan, E.C., Chaudhri, M.M., Sherwood, J.N.,
770 Beard, B.C., 1992. The identification of bonding agents for TATB/HTPB polymer bonded explosives.
771 Philosophical Transactions of the Royal Society A 339, 321-333.
772 Banerjee, B., Adams, D.O., 2004. On predicting the effective elastic properties of polymer bonded
773 explosives using the recursive cell method. International Journal of Solids and Structures 41, 481-
774 509.
775 Barua, A., Horie, Y., Zhou, M., 2012a. Energy localization in HMX-Estane polymer-bonded explosives
776 during impact loading. Journal of Applied Physics 111, 054902.
777 Barua, A., Horie, Y., Zhou, M., 2012b. Microstructural level response of HMX-Estane polymer-bonded
778 explosive under effects of transient stress waves. Proceedings of the Royal Society A: Mathematical,
779 Physical and Engineering Sciences 468, 3725-3744.

780 Barua, A., Zhou, M., 2011. A Lagrangian framework for analyzing microstructural level response of
781 polymer-bonded explosives. Modelling and Simulation in Materials Science and Engineering 19,
782 055001.
783 Brouwers, H.J.H., 2006. Particle-size distribution and packing fraction of geometric random packings.
784 Physical Review E 74.
785 BSI, 2012. BS EN ISO 527-2:2012 Plastics -Determination of tensile properties, Part2: Test conditions
786 for moulding and extrusion plastics, BSI Standards Publication.
787 BSIb, 2012. BS EN 933-1:2012 Test for geometrical properties of aggregates. Determination of
788 particle size distribution. Sieving method., BSI Standard Publications.
789 Cady, W.E. and Caley, L.E., 1977. Properties of Kel F-800 polymer. Lawrence Livermore Laboratory
790 UCRL-52301.
791 Connors, S.C., 2014. The effects of gamma radiation on a PBX containing TATB and the
792 fluoropolymer FK-800, Cranfield Deference and Security. Cranfield University.
793 Drodge, D.R., Williamson, D.M., Palmer, S.J.P., Proud, W.G., Govier, R.K., 2010. The mechanical
794 response of a PBX and binder: combining results across the strain-rate and frequency domains.
795 Journal of Physics D: Applied Physics 43, 335403.
796 Drozdov, 1999. Modeling viscoelastic response of particulate polymeric composites with high
797 volume fractions of fillers. Mathematical and Computer Modelling 29, 11-25.
798 Ellis, K., Leppard, C., Radesk, H., 2005. Mechanical properties and damage evaluation of a UK PBX.
799 Journal of Materials Science 40, 6241-6248.
800 Gee, R.H., Maiti, A., Bastea, S., Fried, L.E., 2007. Molecular dynamics investigation of adhesion
801 between TATB surfaces and amorphous fluoropolymers. Macromolecules 40, 3422-3428.
802 Guo, H., Luo, J.-r., Shi, P.-a., Xu, J.-g., 2014. Research on the fracture behavior of PBX under static
803 tension. Defence Technology 10, 154-160.
804 Gusev, A. A. (2016). Controlled accuracy finite element estimates for the effective stiffness of
805 composites with spherical inclusions. International journal of solids and structures, 80, 227-236.
806 Hagan, E.W.S., Charalambides, M.N., Young, C.R.T., Learner, T.J.S., Hackney, S., 2011. Influence of
807 the inorganic phase concentration and geometry on the viscoelastic properties of latex coatings
808 through the glass-transition. Polymer 52, 1662-1673.
809 Hashin, Z., Shtrikman, S., 1963. A variational approach to the theory of the elastic behaviour of
810 multiphase materials. Journal of Mechanics and Physics of Solids 11, 127-140.
811 Herrmann, H.J., Mahmoodi Baram, R., Wackenhut, M., 2003. Searching for the perfect packing.
812 Physica A: Statistical Mechanics and its Applications 330, 77-82.
813 Herrmann, M., Förter-Barth, U., Bohn, M.A., Krause, H., Koch, M., Arnold, W., 2015. Microstructure
814 of the HMX-Based PBX KS32 after Mechanical Loading. Propellants, Explosives, Pyrotechnics 40, 880-
815 885.
816 Hoffman, D.M., Matthews, F.M. and Pruneda, C.O., 1989. Dynamic mechanical and thermal analyiss
817 of crystallinity development in Kel-F 800 and TATB/Kel-F 800 plastic bonded explosives. Part I. Kel-F
818 800, Thermochimica Acta, 156, 365-372.
819 Jalocha, D.A., A.; Constantinescu, A.; Neviere, R.;, 2013. On the identification of nonlinear behaviour
820 of highly filled elastomer, 11e Colloque National en Calcul des Structures, Giens, France, pp. 1-8.
821 Kansal, A.R.T., Salvatore; Stillinger, Frank H.;, 2002. Diversity of order and densities in jammed hard-
822 particle packings. Physical Review E 66, 1-8.
823 Li, M., Zhang, J., Xiong, C.Y., Fang, J., M Li, J., Hao, Y., 2005. Damage and fracture prediction of
824 plastic-bonded explosive by digital image correlation processing. Optics and Lasers in Engineering 43,
825 856-868.
826 Lielens, G., Pirotte, P., Couniot, A., Dupret, F., Keunings, R., 1998. Prediction of thermo-mechanical
827 properties for compression moulded composites. Composites Part A 29A, 63-70.
828 Lin, C., He, G., Liu, J., Huang, Z., Pan, L., Zhang, J., Liu, S., 2015. Enhanced non-linear viscoelastic
829 properties of TATB-based polymer bonded explosives filled with hybrid graphene/multiwalled
830 carbon nanotubes. RSC Adv. 5, 94759-94767.

831   Lin, S.C., Yang, C.C., Mura, T., Iwakuma, T., 1992. Average elastic-plastic behaviour of composite
832   materials. International Journal of Solids and Structures 29, 1859-1872.
833   Liu, Z.W., Xie, H.M., Li, K.X., Chen, P.W., Huang, F.L., 2009. Fracture behavior of PBX simulation
834   subject to combined thermal and mechanical loads. Polymer Testing 28, 627-635.
835   Ma, X., Zhao, F., Ji, G., Zhu, W., Xiao, J., Xiao, H., 2008. Computational study of structure and
836   performance of four constituents HMX-based composite material. Journal of Molecular Structure:
837   THEOCHEM 851, 22-29.
838   Marvi-Mashhadi, M., Lopes, C.S.,Llorca, J., 2018a, "Modelling of the mechanical behavior of
839   polyurethane foams by means of micromechanical characterization and computational
840   homogenization", International Journal of Solids and Structures 146, 154–166.
841   Marvi-Mashhadi, M., Lopes, C.S.,Llorca, J., 2018b, " Effect of anisotropy on the mechanical
842   properties of polyurethane foams: An experimental and numerical study", Mechanics of Materials
843   124, 143-154.
844   Mohammed, M.A.P., Tarleton, E., Charalambides M.N. and Williams, J.G., 2013, " Mechanical
845   characterization and micromechanical modeling of bread dough", J Rheol 57, 249-272.
846   Mori, T., Tanaka, K., 1973. Average stress in matrix and average elastic energy of materials with
847   misftitting inclusions. Acta Metallurgica 21, 571-574.
848   Qin, Q.H., Yang, Q.-S., 2008. Macro-micro theory on multifield coupling behaviour of heterogeneous
849   materials. Higher Education Press, Beijing and Springer-Verlag GmbH Berlin Heidelberg.
850   Qin, H., Yan, B-L., Zhong, M., Jiang, -L., Liu, F-S., Tang, B. and Liu, Q-J., 2019, First-principles study of
851   structural, elastic, and electronic properties of triclinic TATB under different pressures, Physica B:
852   Condensed Matter 552 , 151-158.
853   Rae, P.J., Goldrein, H.T., Palmer, S.J.P., Field, J.E., Lewis, A.L., 2002. Quasi-static studies of the
854   deformation and failure of β-HMX based polymer bonded explosives. Proceedings of the Royal
855   Society London A 458, 743-762.
856   Reuss, A., 1929. Berechnung der Fließgrenze von Mischkristallen auf Grund der Plastizitätsbedingung
857   für Einkristalle. Zeitschrift für Angewandte Mathematik und Mechanik 9, 49-58.
858   Roskilly, S.J., Colbourn, E.A., Alli, O., Williams, D., Paul, K.A., Welfare, E.H. and Trusty, P.A., 2010.
859   Investigating the effect of shape on particle segregation using a Monte Carlo simulation. Poweder
860   Technology 203, 211-222.
861   Saeb, S., Steinmann, P., Javili, A., 2016. Aspects of computational homogenization at finite
862   deformations: A unifying review from Reuss' to Voigt's Bound. Applied Mechanics Reviews 68,
863   050801-1.
864   Seidel, G.D., Allen, D.H., Helms, K.L.E., Groves, S.E., 2005. A model for predicting the evolution of
865   damage in viscoelastic particle-reinforced composites. Mechanics of Materials 37, 163-178.
866   Skamniotis, C.G., Elliott, M., Charalambides, M.N., 2019. On modelling the constitutive and damage
867   behaviour of highly non-linear bio-composites – Mesh sensitivity of the viscoplastic damage
868   law computations. Int J Plasticity 114, 40-62.
869   Skidmore, C.B., Phillips, D.S., Asay, B.W., Idar, D.J., Howe, P.M. and Bolme D. S., 1998.
870   Microstructural effects in PBX 9501 damaged by shear Impact, LA-UR-99-3233, Los Alamos National
871   Laboratory, Los Alamos, New Mexico 87545, USA.
872   Stapountzi, O.A., Charalambides, M.N., Williams, J.G., 2009. Micromechanical models for stiffness
873   prediction of alumina trihydrate (ATH) reinforced poly (methyl methacrylate) (PMMA): Effect of filler
874   volume fraction and temperature. Composites Science and Technology 69, 2015-2023.
875   Talawar, M.B., Agarwal, A.P., Anniyappan, M., Gore, G.M., Asthana, S.N., Venugopalan, S., 2006.
876   Method for preparation of fine TATB (2-5 microm) and its evaluation in plastic bonded explosive
877   (PBX) formulations. Journal of hazardous materials 137, 1848-1852.
878   Tan, H., Huang, Y., Geubelle, P., 2005. An energy approach to a micromechanics model accounting
879   for nonlinear interface debonding, 41st AIAA/ASME/SAE/ASEE Joint Propulsion Conference & Exhibit,
880   Tucson, Arizona.
881   Tarleton, E., Charalambides, M.N., Leppard, C., 2012. Image-based modelling of binary composites.
882   Computational Materials Science 64, 183-186.

Tarleton, E., Charalambides, M.N., Leppard, C., Yeoh, J.L., 2013. Micromechanical modelling of alumina trihydrate filled poly (methyl methacrylate) composites. Int J Materials and Structural Integrity 7, 31-47.

Trombini, M., Nadot-Martin, C., Halm, D., Gueguen, M., Contesse, G., Fanget, A., 2015. Multiscale damage modeling with the "Morphological Approach" to highlight particle size and interaction effects in highly-filled particulate composites. European Journal of Mechanics - A/Solids 53, 163-174.

Voigt, W., 1889. Ueber die Beziehung zwischen den beiden Elasticitätsconstanten isotroper Körper. Annalen der Physik 274, 573-587.

Wang, X., Ma, S., Zhao, Y., Zhou, Z., Chen, P., 2011. Observation of damage evolution in polymer bonded explosives using acoustic emission and digital image correlation. Polymer Testing 30, 861-866.

Wang, X., Wu, Y., Huang, F., Jiao, T., Clifton, R.J., 2016. Mesoscale thermal-mechanical analysis of impacted granular and polymer-bonded explosives. Mechanics of Materials 99, 68-78.

Willey, T.M., Hoffman, D.M., van Buuren, T., Lauderbach, L., Gee, R.H., Maiti, A., Overturf, G.E., Fried, L.E., Ilavsky, J., 2009. The Microstructure of TATB-Based Explosive Formulations During Temperature Cycling Using Ultra-Small-Angle X-Ray Scattering. Propellants, Explosives, Pyrotechnics 34, 406-414.

Williamson D.M., Hamilton N.R., Jardine A.P., 2017. Rate Dependent Interfacial Properties Using the JKR Experimental Technique. In: Antoun B. et al. (eds) Challenges in Mechanics of Time Dependent Materials, Volume 2. Conference Proceedings of the Society for Experimental Mechanics Series. Springer, Cham

Williamson, D.M., Siviour, C.R., Proud, W.G., Palmer, S.J.P., Govier, R., Ellis, K., Blackwell, P., Leppard, C., 2008. Temperature–time response of a polymer bonded explosive in compression (EDC37). Journal of Physics D: Applied Physics 41, 085404.

Wood, D.C., Appleby-Thomas, G.J., Fitzmaurice, B.C., Hameed, A., Millett, J.C.F. and Hazell, P.J., 2017. On the shock response of PCTFE (Kel-F 81), AIP Conference Proceedings 1793, 050005: https://doi.org/10.1063/1.4971539

Wu, Y.-Q., Huang, F.-L., 2009. A micromechanical model for predicting combined damage of particles and interface debonding in PBX explosives. Mechanics of Materials 41, 27-47.

Xiao, J., Huang, Y., Hu Y. and Xiao, H., 2005. Molecular dynamics simulation of mechanical properties of TATB/fluorine-polymer PBXs along different surfaces, Science in China Ser. B Chemistry, Vol.48 No.6 504—510.

Xiao, J., Ma, X., Zhu, W., Huang, Y., Xiao, H., 2007. Molecular Dynamics Simulations of Polymer-Bonded Explosives (PBXs): Modeling, Mechanical Properties and their Dependence on Temperatures and Concentrations of Binders. Propellants, Explos., Pyrotech. 32, No. 5, 355 – 359.

Xiao, J.J., Wang, W.R., Chen, J., Ji, G.F., Zhu, W., Xiao, H.M., 2012. Study on structure, sensitivity and mechanical properties of HMX and HMX-based PBXs with molecular dynamics simulation. Computational and Theoretical Chemistry 999, 21-27.

Xu, F., Aravas, N., Sofronis, P., 2008. Constitutive modeling of solid propellant materials with evolving microstructural damage. Journal of the Mechanics and Physics of Solids 56, 2050-2073.

Yeager, J.D., 2011. Microstructural characterization of simulated plastic-bonded explosives, School of Mechanical and Materials Engineering. Washington State University.

Yeager, J.D., Ramos, K.J., Hooks, D.E., Majewski, J., Singh, S., 2014. Formulation-derived interface characteristics contributing to failure in plastic-bonded explosive materials, 15th International Detonation Symposium, San Francisco, California, United States.

Zhang, R., Li-Mayer, J.Y.S. and Charalambides M.N., 2018. Development of an image-based numerical model for predicting the microstructure–property relationship in alumina trihydrate (ATH) filled poly(methyl methacrylate) (PMMA), Int J Fract 211, 125-148.

Zhou, Z., Chen, P., Duan, Z., Huang, F., 2011. Comparative study of the fracture toughness determination of a polymer-bonded explosive simulant. Engineering Fracture Mechanics 78, 2991-2997.

934